

## $\rho$ Production and Decay in the Reaction $\pi^- p \rightarrow \pi^- \pi^0 p$ at 5 GeV/c\*

L. Byerly,† R. Anthony,‡ C. T. Coffin, E. Meanley,§ D. I. Meyer, J. Rice,||  
N. R. Stanton,\*\* and K. M. Terwilliger

Physics Department, University of Michigan, Ann Arbor, Michigan 48104

(Received 12 June 1972)

Production and decay distributions of  $\rho^-$  from  $\pi^- p \rightarrow \pi^- \pi^0 p$  have been measured in an optical spark chamber experiment at 5 GeV/c. About 3000 events are obtained with  $610 \leq \omega$  (dipion mass)  $\leq 910$  MeV/c<sup>2</sup> and  $-0.04 \geq t \geq -0.35$  (GeV/c)<sup>2</sup>. Our data, and  $\rho^-$  and  $\rho^0$  data from other experiments, are used to study the  $\omega$  and  $t$  dependences of the helicity-frame cross sections. We find that (1)  $\rho_{00}^H d\sigma/dt$  and  $\text{Re}\rho_{10}^H d\sigma/dt$  are the same for  $\rho^-$  and  $\rho^0$  production except for an over-all normalization factor (2) the  $\omega$  distributions of  $\rho_{11}^H d\sigma/dt$  and  $\rho_{1-1}^H d\sigma/dt$  for  $\rho^-$  are strongly skewed toward low values of  $\omega$  while the corresponding distributions for  $\rho^0$  are not. The first result is shown to be reasonable in the context of a model assuming  $\pi$  and  $\omega^0$  exchange and absorption effects. We have not been able to explain the second result. The forward-backward asymmetry of the  $\rho^-$  decay from this experiment is significantly smaller than values from some other experiments between 2.5 and 8 GeV/c.

### I. INTRODUCTION

The production and decay characteristics of the  $\rho^-$  meson in the reaction

$$\pi^- p \rightarrow \pi^- \pi^0 p \quad (1)$$

have been studied in a number of bubble-chamber experiments at incident  $\pi^-$  momenta up to 8 GeV/c.<sup>1-12</sup> This reaction is of interest because the dynamics are expected to be relatively simple if the dominant production mechanism is the exchange of a single pion. Considerable theoretical effort has gone into the study of reaction (1), and to the characteristics of  $\rho^0$  mesons produced in the reaction

$$\pi^- p \rightarrow \pi^- \pi^+ n. \quad (2)$$

The most successful treatment of these reactions has come from the absorption modified one-pion-exchange (OPEA) model.<sup>13</sup> Indeed, this model gives a very good description<sup>14</sup> of the low-momentum-transfer dynamics of reaction (2) up to an incident pion momentum of 15 GeV/c.

Reaction (1) is not as well understood as reaction (2). There is clear evidence<sup>7,9,10</sup> that for incident  $\pi^-$  momenta above 4 GeV/c, the  $\rho^-$  production and decay distributions in reaction (1) are not consistent with OPEA. This is not surprising since it has been known for some time that exchanges other than  $\pi$  exchange may be important for  $\rho$  production.<sup>15</sup> Since  $\omega^0$  is the most important exchange that can contribute to  $\rho^-$  production, but not to  $\rho^0$  production, it has been assumed to be

responsible for deviations of  $\rho^-$  cross sections from OPEA behavior. While the inclusion of  $\omega^0$  exchange has made it possible to fit  $\rho^-$  decay distributions,<sup>7,9,10</sup> the role of this exchange in  $\rho^-$  production has not been clearly established because of the low statistical accuracy of the data. The experimental situation below 4 GeV/c is even less clear. Malamud and Schlein<sup>11</sup> give evidence based on one high-statistics bubble-chamber compilation that some exchange mechanism in addition to  $\pi$  exchange is important between 2 and 3 GeV/c, while Scharenguivel *et al.*<sup>12</sup> find from another compilation that  $\pi$  exchange is sufficient.

In this paper we will show that  $\omega^0$  exchange (or some other non- $\pi$  exchange) does have an important effect on  $\rho^-$  production and decay distributions at 5 GeV/c and probably does also between 2 and 3 GeV/c. This will be done by examining the measured dependence of  $\rho^-$  and  $\rho^0$  decay density-matrix elements on dipion mass,  $\omega$ , and production four-momentum transfer squared  $t$ . We find that the partial cross sections in the helicity frame  $\rho_{00}^H d\sigma/dt$  and  $\text{Re}\rho_{10}^H d\sigma/dt$  (defined in Sec. IX) for  $\rho^-$  decay are consistent with those for  $\rho^0$  decay, while the cross sections  $\rho_{11}^H d\sigma/dt$  and  $\rho_{1-1}^H d\sigma/dt$  for  $\rho^-$  are quite different from those  $\rho^0$  decay. We will also show that while some features of this situation can be qualitatively explained by assuming absorbed  $\omega^0$  exchange, the most interesting feature is not explained by conventional models; this is, that for reaction (1), the cross sections  $\rho_{11}^H d\sigma/dt$  and  $\rho_{1-1}^H d\sigma/dt$  have superimposed on the usual  $\rho$  resonance shape, a factor that decreases rapidly with increasing  $\omega$ .

## II. EXPERIMENTAL APPARATUS AND PROCEDURE

Counter-controlled spark chambers were used as detectors in this experiment so that we could collect a large sample of  $\rho^-$  events from reaction (1) at a relatively high energy. We chose not to include any information from the  $\rho^-$  decay products in the trigger in order that there should be no bias in the measured decay distributions. Thus our trigger was based essentially on detection (in coincidence) of the projectile  $\pi^-$  and recoil proton of reaction (1). This combination is convenient because of the particular kinematics of reaction (1); for dipion masses near the  $\rho$  mass, and for small momentum transfer, the recoil proton is slow and is produced nearly sideways from the incident beam direction. This is shown quantitatively in Fig. 1 where the lab polar angle between the recoil proton and the projectile pion is plotted vs  $-t$  (squared four-momentum transfer from the target proton to the recoil proton) for several values of dipion mass,  $\omega$ . Figure 1 shows that a detector subtending only a modest proton lab angle can cover much of the ranges of  $t$  and  $\omega$  appropriate to the study of peripheral production of  $\rho$  mesons. Moreover, the proton kinetic energy,  $T_p$ , in this kinematic region, is small enough that the proton velocity (determined by time-of-flight measurement) can be used to discriminate between protons and relativistic particles produced in  $\pi^-p$  interactions.

Figure 2 shows a schematic layout of our apparatus with a typical event from reaction (1) superimposed on it. The apparatus was located in the  $17^\circ$  beam of the Argonne National Laboratory ZGS. As indicated above, the spark chambers were triggered essentially on a coincidence

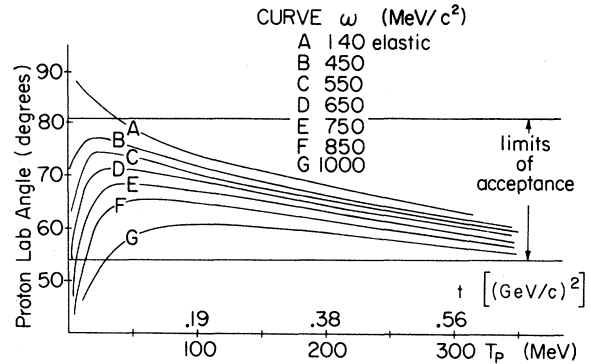


FIG. 1. Proton laboratory angle as a function of proton kinetic energy for various values of the mass,  $\omega$ , of  $X$  in the reaction  $\pi^-p \rightarrow X^- + p$ .

between a pulse from the proton counter and a delayed pulse from the interacting beam coincidence  $C_1C_2C_3C_4$ . The rest of the apparatus of Fig. 2 was used to record enough kinematic information to identify any event from reaction (1). The type of information obtained on the final state  $\pi^-$  and  $\pi^0$  depends on the decay configuration of the dipion. The direction of the final  $\pi^-$  is always recorded since for  $\omega < 1100$  MeV/c<sup>2</sup> the  $\pi^-$  is kinematically constrained to go through chambers 5 and 6. If the  $\pi^-$  carries away one half or more of the available dipion energy, it is constrained to go through the full spectrometer and its momentum can be measured. If the  $\pi^0$  carries away one half or more of the dipion energy, its decay  $\gamma$  rays will produce measurable showers in chambers 7 and 8 after the lead plate (with about 80% probability). There are, of course, some events for which all of the information indicated above is obtained. These events were used to determine the  $\gamma$ -ray conversion efficiency in a manner de-

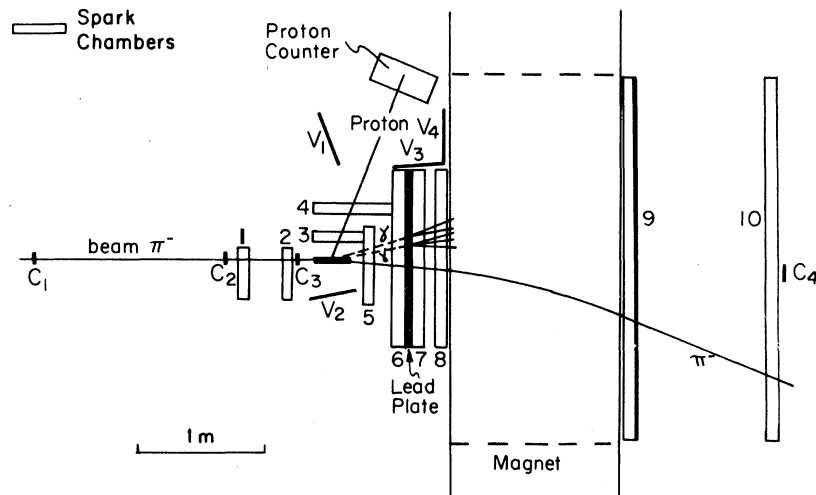


FIG. 2. Top view of experimental apparatus.

scribed in Sec. V.

In order to guarantee that the final  $\pi^-$  momentum could be measured over the energy range described above, and for all dipion decay configurations, it was necessary that the magnet aperture be designed to accept pions at large angles to the beam direction. With the Argonne SCM 105 magnet used in this experiment, a sufficiently large angular acceptance could be obtained only by raising the magnet so that most of the gap was above the median plane of the apparatus. For this reason, only events where the  $\pi^-$  goes above the production plane are included in the final  $\rho^-$  decay distributions. Our distributions nevertheless contain all of the available information since invariance of the cross sections under reflection through the production plane makes it unnecessary to observe events where the  $\pi^-$  goes below the production plane.

Since our apparatus was triggered on the recoil proton, we were not able to observe events with very small  $|t|$ . The recoil protons require a kinetic energy,  $T_p$ , of from 20 to 40 MeV, depending on their point of origin in the liquid hydrogen target, to escape the target and produce a pulse

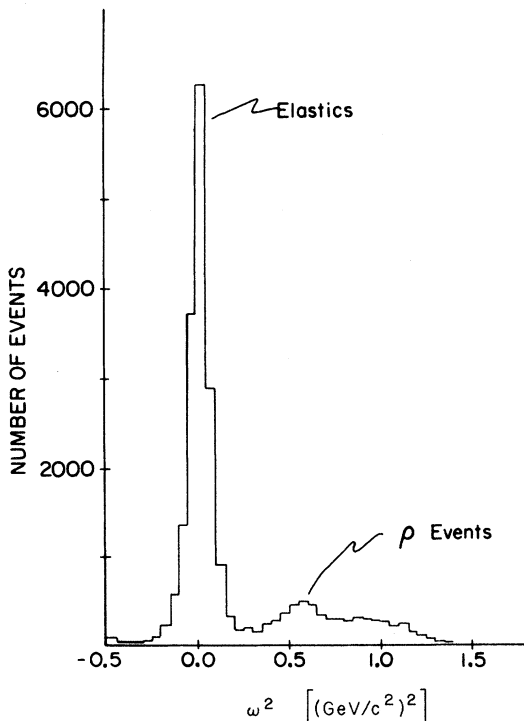


FIG. 3. Distribution of events in squared missing mass,  $\omega^2$ , as calculated from the recoil proton momentum after the preliminary scanning.  $\omega$  is the effective mass of  $X$  in the reaction  $\pi^- p \rightarrow X^- p$ . This histogram contains only one fifth of the total data of the experiment.

in the proton counter. As a result, we do not observe events with  $|t| = 2M_p T_p$  less than about  $0.05$   $(\text{GeV}/c)^2$ . On the other hand, for  $T_p > 200$  MeV, the time-of-flight resolution of the proton counter ( $\sim 1.2$  nsec full width at half maximum) is no longer sufficient to clearly identify the type of event, so we do not use events with  $|t| > 0.4$   $(\text{GeV}/c)^2$ .

The range of dipion mass that we observe is also limited by the proton counter. The horizontal lines on Fig. 1 show the extreme polar angles possible for protons originating at any point of the hydrogen target and reaching any point of the proton counter. As can be seen from Fig. 1, we do not observe events with  $\omega \geq 1200$   $\text{MeV}/c^2$ .

All of the information associated with each event was recorded on a single frame of 35-mm film. This included horizontal and vertical views of the spark chambers and several sets of panel lights containing a digitized record of the time of flight and pulse height from the proton counter. About 400 000 pictures were taken in all. As a final remark, we mention that the veto counters V1 through V4, shown in Fig. 2, were used to suppress background from interactions taking place outside the hydrogen target.

### III. PRELIMINARY EVENT SELECTION

Since only a small fraction of the 400 000 pictures taken contained interesting events, we used the Michigan Automatic Scanning System, MASS,<sup>18</sup> to make a rapid prescan that eliminated many of the unwanted events. In the prescan, the tracks in the beam and recoil proton spark chambers were measured and the proton time-of-flight lights

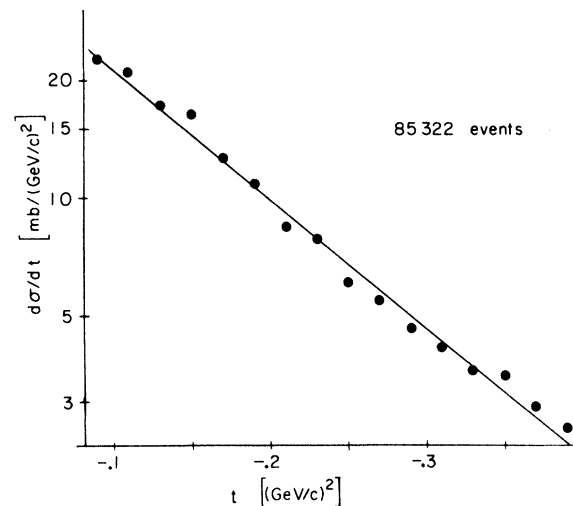


FIG. 4. Elastic differential cross section. The straight line is the best fit of an  $A \exp(Bt)$  form to the data.

were read. We rejected all frames that had more than one track in the beam chambers and all frames for which the event origin was not in the liquid hydrogen target. There remained 221 000 events. For each of these events we computed  $t$  and  $\omega$  (the invariant mass of all final-state particles except for the proton. Events with  $|t| > 0.40$   $(\text{GeV}/c)^2$  were cut from the sample due to the poor resolution in the proton velocity measurement for such events. Figure 3 shows the distribution in  $\omega^2$  for a typical sample containing about one fifth of the data of the experiment. It can be seen that the elastic events centered in the peak at  $\omega^2 = 0.02$   $(\text{GeV}/c^2)^2$  make up about 80% of this sample, and that the elastic peak overlaps the lower part of the inelastic region. The cutoff in events above 1.1  $(\text{GeV}/c^2)^2$  is due primarily to the geometry of the hydrogen target and proton counter as was explained in Sec. II.

To avoid having to measure further the large number of elastic events in the data, all events with missing mass squared less than 0.3  $(\text{GeV}/c^2)^2$  were considered to be elastic and cut from the sample of events which were to be completely measured. While it is clear that some inelastic events are included in these "elastic" events and that some real elastic events are included in the inelastic region, these errors were found to be only of the order of a few percent. About 25 000 candidates for  $\rho$  events survived this cut on  $\omega^2$ .

The elastic events from the  $\omega^2$  cut were used as a check on our method of analysis. Figure 4 shows the elastic differential cross section computed as a function of  $t$  for the entire experiment. Each event has been weighted to account for the azimuthal acceptance of the proton counter and amount of target available for that event configuration. There are no data points in Fig. 4 for  $|t| < 0.08$   $(\text{GeV}/c)^2$  because the geometry of the experiment excludes such events. A fit of the form  $A \exp(Bt)$  to the data of Fig. 4 gives  $A = 48.4 \pm 2.6$   $\text{mb}/(\text{GeV}/c)^2$  and  $B = 7.88 \pm 0.25$   $(\text{GeV}/c)^{-2}$ , values

that agree well with the results from other experiments at this energy.<sup>17</sup> While the normalization and average  $t$  dependence of our data are accurate to  $\sim 5\%$ , there may be some small deviations from the correct distributions over a  $t$  range of  $\sim 0.02$   $(\text{GeV}/c)^2$ . Some of the data points of Fig. 4 deviate more from an exponential fit than their statistical errors (about the size of the circles) would allow. We have not been able to find an instrumental cause for these deviations.

#### IV. FINAL-EVENT SELECTION

The events with  $\omega^2 > 0.3$   $(\text{GeV}/c^2)^2$  were completely rescanned and measured by human scanners. It was necessary to use human scanners for the spark chambers downstream of the hydrogen target because multiple tracks in these chambers often caused a track quality too poor for the automatic scanner. The human scanners rejected all events having more than, or less than, one charged particle track in chambers 5 and 6 (see Fig. 2). This cut reduced the number of events from 25 000 to 14 000.

On all remaining events the following measurements were made: (a) final-state  $\pi^-$  tracks in chambers 5 and 6, (b)  $\pi^-$  tracks through the magnet chambers (if possible), and (c) positions of  $\gamma$  showers (if possible). Each measured event was classified as belonging to one of six types depending on the kind of measurements made. Table I summarizes the labels used for each event type, the measurements made for each type, and the number of events of each type observed in the experiment.

It can be seen from Table I that there are about twice as many events with one measured  $\gamma$  shower as there are with two measured showers. This is to be contrasted with the expected ratio of one  $\gamma$  to two  $\gamma$  conversions in the lead plate which is about  $\frac{1}{2}$ . There were primarily two effects that made the measurement of more than one  $\gamma$  shower

TABLE I. Types of events for hand scanning. The type assigned each event corresponds to the measurements available for that event.

Type	Measurements made		Number of events observed	Number of constraints in fit to $\rho$ hypothesis	Maximum $\chi^2$ for accepted $\rho$ events
	$\pi^-$ track through magnet	Number of $\gamma$ showers			
1	Yes	2	1102	3	15
2	Yes	1	2010	3	10
3	Yes	0	3766	1	5
7	No	2	1986	2	4
8	No	1	3561	2	4
9	No	0	1276	0	

difficult. First, a spark was often obliterated by "spark robbing" from another track nearby. Second, shower tracks were sometimes confused by the appearance of additional tracks due to shower particles that were reflected by the magnet. While we are therefore not able to predict *a priori* the probabilities for observing different event types, we can measure these probabilities by studying events that can be identified without using the  $\gamma$  showers. Our procedure for doing this is described in the next section under the heading of efficiency corrections. These efficiency corrections allow us, among other things, to estimate the number of good reaction (1) events among the unconstrained type-9 events listed in Table I. Consequently, we reject all type-9 events at this point and do not consider them further.

Since each event type is identified by different kinds of measurements, the background from channels other than reaction (1) is different for each type. The major contributors to the background are the two reactions

$$\pi^- p \rightarrow \pi^- p \quad (3)$$

and

$$\pi^- p \rightarrow \pi^- p + 2\pi^0. \quad (4)$$

In the rest of this section we describe our determination of the background corrections for the various event types.

Of the five types remaining after rejection of type 9, only type 3 can be simulated by elastic scattering; there are no  $\gamma$  showers in this case. Since elastic scatterings are much more numerous than  $\rho$  events, a relatively small fraction of elastic events having  $\omega^2 > 0.3$  (GeV/c<sup>2</sup>)<sup>2</sup> (probably

due to the proton's suffering a second interaction) can cause a significant background in the  $\rho$  events. To eliminate these elastic events, all type-3 events were first fitted to the elastic hypothesis *ignoring the proton information*; this is a 1-C fit. Figure 5 shows the resulting distribution of  $\chi^2$  values. The peak for small  $\chi^2$  shows the presence of elastic events. The dashed line shows the Monte Carlo generated shape of the background in this  $\chi^2$  distribution assuming that it is due to reaction (1); the solid line shows the background distribution which, when subtracted from the measured  $\chi^2$  distribution leaves a classical 1-C shape for the elastic events. The rough agreement between the solid and dashed lines gives us confidence that, having rejected all events with  $\chi^2 < 1.0$ , we know how many reaction (1) events are lost and elastics accepted by this cut. Approximately 700 of the 3766 type-3 events were eliminated by the cut.

All remaining events in the sample were fitted to the reaction (1) hypothesis. In order to simplify the fitting procedure for events having only one  $\gamma$  shower (types 2 and 8), we note that the opening angle of the two  $\gamma$  rays from the  $\pi^0$  decay is very small for energetic  $\pi^0$ 's. It is then reasonable to assume that the  $\pi^0$  was emitted in the direction of the  $\gamma$  shower and to compensate for the approximation by assigning an angular error, proportional to the opening angle, to the  $\pi^0$  direction. The number of constraints is then the same for one- and two-shower events as is indicated in Table I.

We show the  $\chi^2$  distributions for the fits of types 1 and 8 events in Figs. 6 and 7; we present these distributions because they show the extremes of background levels. To determine the background correction for each type, we first verify that the  $\chi^2$  distributions have the correct shape for small  $\chi^2$ , where reaction (1) events dominate, and for large  $\chi^2$  where reaction (4) events are assumed to dominate. Only for type-3 events, where there are no  $\gamma$  showers, do the  $\chi^2$  distributions have the classical shapes expected for Gaussian error distributions. Since the errors in the  $\gamma$  shower measurement are not Gaussian distributed, we have used a Monte Carlo technique to find the expected  $\chi^2$  shapes for reaction (1) and reaction (4) events fitted to the reaction (1) hypothesis. The error distribution for  $\gamma$  showers was determined experimentally by studying the distribution in shower position near an opening (beam exit hole) in the lead plate. The Monte Carlo generated  $\chi^2$  distributions agree well with the observed  $\chi^2$  distributions for types 1, 2, 7, and 8. Using these distributions, we set the  $\chi^2$  limits given in Table I as most appropriate for each type of reaction (1) event. The solid curves in Figs. 6 and 7 are the

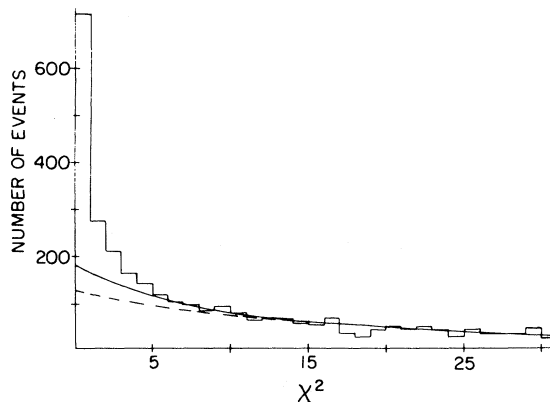


FIG. 5. Distribution of  $\chi^2$  values for the fit of all type-3 events to the elastic hypothesis, ignoring recoil proton momentum. The dashed curve is the Monte Carlo generated background. The solid curve is the distribution for background which leaves a 1-C distribution for elastic events.

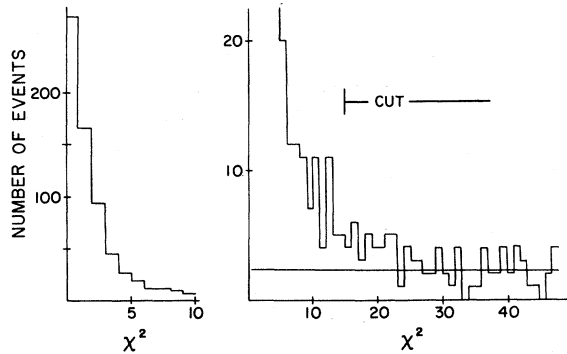


FIG. 6. Distribution of  $\chi^2$  values for the fit of all type-1 events to the reaction (1) hypothesis. The solid line in the enlargement on the right shows the Monte Carlo generated shape of background. All events with  $\chi^2 < 15.0$  were accepted as reaction (1).

expected background distributions normalized at large  $\chi^2$  where there are essentially no events from reaction (1). The background corrections are almost insignificant except for type-7 and type-8 events where the  $\gamma$  showers are essential for identification. For type-7 and type-8 events together, 8% of the events accepted are background and 13% of the real events are lost. This fraction of real events lost is checked by an independent method in the next section.

To test our assumption that most background is from reaction (4), we examine the distribution in  $\omega^2$  for events rejected by the cuts described above. These distributions are shown for each event type in Fig. 8. They agree well with the missing-mass distribution observed for reaction (4) in bubble-chamber experiments at about the same energy.<sup>7</sup> Of course, our missing-mass distributions cut off artificially above  $1.1 \text{ (GeV}/c^2)^2$  due to the geometrical limit of the experiment. The rejected type-3 events obviously contain a number of elastic events, as is expected. The rejected type-8 events show a strong  $\rho$  peak, which again is expected since from the distributions in Fig. 7 it is estimated that nearly 50% of the rejected events belong to reaction (1).

#### V. CORRECTIONS TO THE DATA

Many reaction (1) events which our apparatus would have ideally detected are missing from the final sample of 8300 events. That this is true is obvious from the large number of type-9 events, lacking sufficient measurements for identification. We have divided these losses into four categories labeled efficiency losses, hole losses, veto losses, and normalization losses. The efficiency losses include losses due to inelastic interactions of the

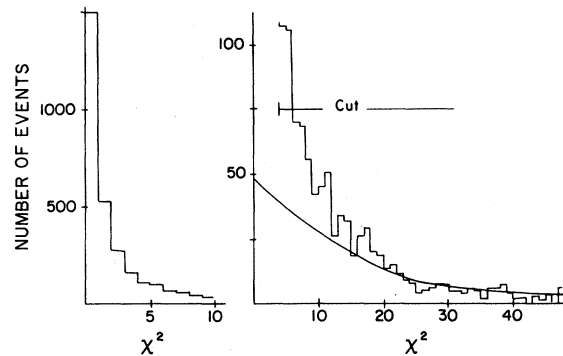


FIG. 7. Distribution of  $\chi^2$  values for the fit of all type-8 events to the reaction (1) hypothesis. The solid curve in the enlargement on the right shows the Monte Carlo generated shape of the background. All events with  $\chi^2 < 4.0$  were accepted as reaction (1).

$\pi^-$  in the lead plate, the failure of  $\gamma$  rays to convert, poor spark quality, and poor scanner measurements. The hole losses are those events lost when the  $\gamma$  rays go through a beam exit hole in the lead plate; the veto losses are those cases where the picture of a reaction (1) event was not taken because one of the charged particles from the event went through a veto counter. Fortunately, none of these losses are such that we lose all of a particular class of events, i.e., all events of a particular  $t$ , dipion mass, and decay direction. Therefore, we correct for these losses by calcu-

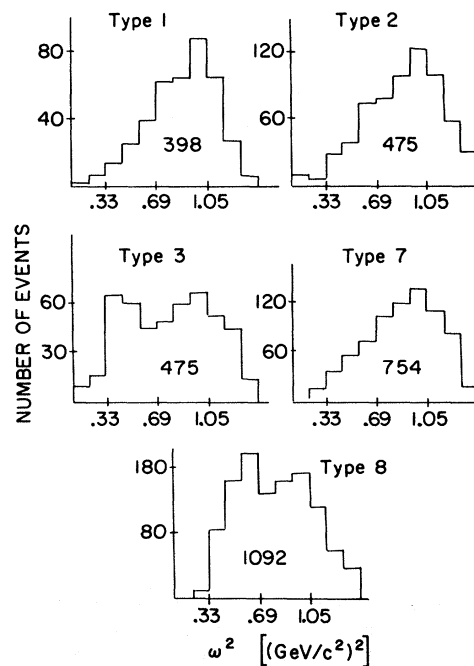


FIG. 8. Distributions of squared missing mass for events rejected by the fits to the reaction (1) hypothesis.

lating weighting factors for each event, where the weight factor is inversely proportional to the probability for observing and identifying that event as a reaction (1) event considering the various loss mechanisms. The normalization losses are due primarily to events rejected when there were two beam pions within the resolving time of the chambers. The correction for this effect is straightforward and has been verified by the correct normalization of the elastic scattering data described in Sec. III.

The efficiency correction for a type-3 event is determined by the chance for the  $\pi^-$  to interact in the lead plate or for the scanners to err in measuring the  $\pi^-$  tracks. This chance is found to be 12.7% by looking at the final-state  $\pi^-$  for a large number of elastic events. An additional 2.6% is added to the type-3 efficiency correction to account for the reaction (1) events lost and background accepted by the  $\chi^2$  cuts. The efficiency corrections for the other types of events are found by studying that subclass of events for which the  $\pi^-$  momentum has been measured to be less than 4.0 GeV/c; these are type-1, -2, and -3 events. By comparing the number of these events that are accepted using only the  $\pi^-$  momentum information (a type-3 fit) against the number that are accepted using only the  $\gamma$  shower information (type-7 and type-8 fits), it is possible to compute the efficiency with which the  $\gamma$  rays convert and are correctly measured. It is found that this efficiency depends somewhat on the laboratory momentum of the  $\pi^0$  and lies between 70 and 80%. In this comparison the fraction of reaction (1) events rejected by the type-1, -2, -7, and -8  $\chi^2$  cuts is computed and is found to agree closely with the fraction computed from the  $\chi^2$  distributions as described at the end of Sec. IV.

A  $1\frac{1}{2}$  by 1 in. rectangular hole was cut in the center of the lead plate (Fig. 2) to allow the beam

to pass. The presence of this hole makes it impossible to identify some of the reaction (1) events which would otherwise have been type-7 or type-8 events. When the most energetic  $\gamma$  rays (or possibly both  $\gamma$  rays) pass through the hole, there is no  $\gamma$  shower and the event is lost. The highest losses are for those events where the  $\pi^0$  has maximum energy and is directed towards the center of the hole. Even for this class of events, the event can be identified 20% of the time, i.e., for 20% of the possible decays of a  $\pi^0$  of a given momentum and direction a  $\gamma$  shower sufficient to identify the event will be produced. For each reaction (1) event that we identify, we compute from the position, direction, and momentum of the  $\pi^0$  the probability of losing that class of event due to the hole, and weight the event accordingly.

It was necessary to use a number of veto counters in this experiment to hold down the number of uninteresting pictures. Several of these veto counters occasionally caused the loss of real reaction (1) events. In Fig. 2 it is seen that it is possible for the final-state  $\pi^-$  to enter C4 (the veto counter intended to detect beam pions) and for the event to be lost. Detailed calculations show this to be an insignificant loss; C4 has only a few square inches of area. However, a second possible loss proves to be quite significant. Positrons produced in  $\gamma$  showers with momenta from 70 to 200 MeV/c can turn around in the magnet and come back through veto counter V4. Due to the strong horizontal component of the magnetic field in this region, the positrons are also bent downward. The net effect is that events with  $\gamma$  showers above the production plane veto themselves out more frequently than events with  $\gamma$  showers below the production plane, because the positrons from the lower  $\gamma$  showers tend to run into the bottom pole face (recall that the magnet was placed asymmetrically in the vertical sense, so that the pro-

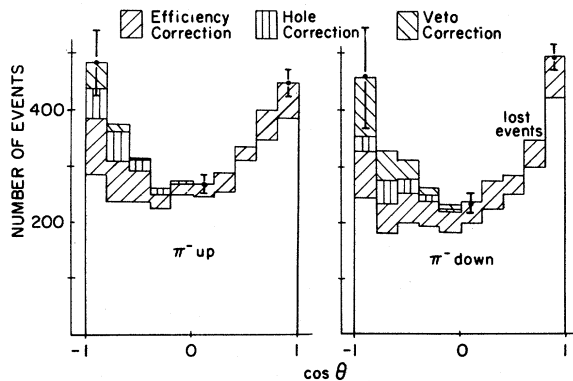


FIG. 9. The effects of the three major corrections on the  $\cos\theta$  distribution for  $\rho$  events in the helicity frame.

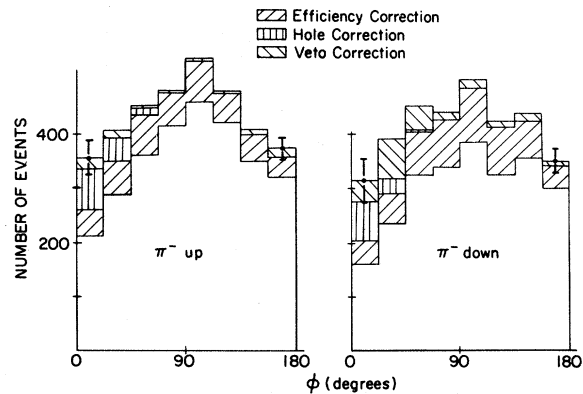


FIG. 10. The effects of the three major corrections on the  $\phi$  distribution for  $\rho$  events in the helicity frame.

duction plane was only 5 in. above the bottom pole face). Before correcting for this loss, we saw a significantly greater number of events with strong  $\gamma$  showers where the final  $\pi^-$  went above the production plane (so  $\gamma$ 's are below) than where the  $\pi^-$  went below the production plane. Using photon shower distribution function tables for lead<sup>18</sup> and a detailed map of the magnetic field, the probability of losing each event was calculated. This probability was never greater than 50% and was considerably less for the events where the  $\pi^-$  is above the production plane, the only events we will use in studying the  $\rho$  decay. All events were weighted to correct for this loss.

Figures 9 and 10 show the effects that each of the three corrections have on the  $\rho$  decay distributions in the  $\rho$  helicity frame. In this frame the  $\rho$  is at rest and the direction of the recoil proton is the negative  $Z$  axis. The angle  $\theta$  is measured from the positive  $Z$  axis and  $\phi$  is measured from the production plane. In both figures two distributions are shown, the distribution of events which have the  $\pi^-$  above the production plane and the distribution of events with the  $\pi^-$  below the production plane. The latter distribution is given only to show how the veto corrections tend to restore symmetry under reflection through the production plane. The events with the  $\pi^-$  down will not be used to compute the density-matrix ele-

ments because the corrections are larger and because there is a kinematic region for which events cannot be observed with high efficiency. For  $\cos\theta$  between 0.4 and 0.8, a  $\pi^-$  heading down is likely to hit the bottom pole face of the magnet and the  $\pi^0$  is produced with too low an energy and at too large an angle to produce good  $\gamma$  showers. The clear histograms below all the hatched areas in Fig. 9 show the distributions seen before any corrections are applied.

## VI. NUCLEON RESONANCE PRODUCTION

In this section we investigate the possibility that resonances in the  $\pi^-p$  and  $\pi^0p$  system may influence the observed properties of the  $\rho^-$ . The  $\rho^-$  decay angular distribution can be particularly sensitive to reflections of the nucleon resonances.

To look for  $\pi p$  resonances in our data, we examine histograms in  $M(\pi^-p)$  and  $M(\pi^0p)$ , the invariant masses of the  $\pi^-p$  and  $\pi^0p$  systems, respectively. These histograms are shown in Figs. 11 and 12. The smooth curve drawn in each histogram is the expected distribution of pion-proton masses calculated from the observed  $\rho$  distributions. The only significant resonancelike structure in these distributions is the single spike in the  $\pi^-p$  distribution at a mass of 1.17  $\text{GeV}/c^2$ . This peak is an instrumental effect. Our correc-

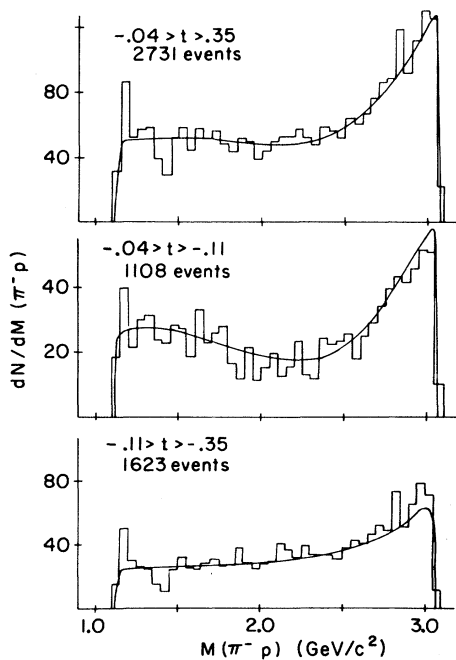


FIG. 11. ( $\pi^-p$ ) mass spectra for events with dipion mass between 660 and 860  $\text{MeV}/c^2$  for different  $t$  intervals. The smooth curves show the mass distributions expected from the reflection of the  $\rho$ .

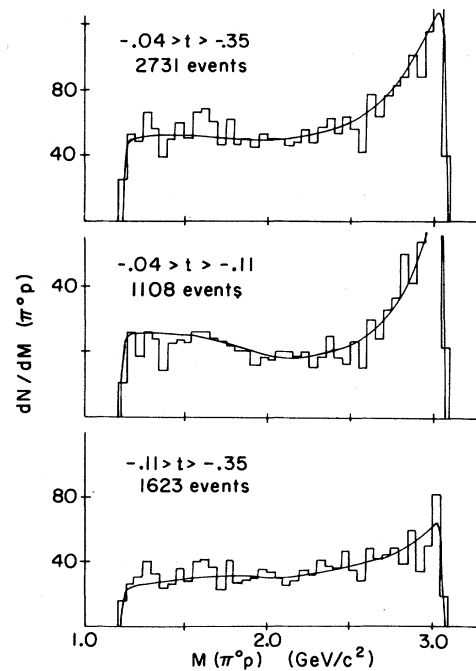


FIG. 12. ( $\pi^0p$ ) mass spectra for events with dipion mass between 660 and 860  $\text{MeV}/c^2$  for different  $t$  intervals. The smooth curves show the mass distributions expected from the reflection of the  $\rho$ .

tion for events lost due to the hole in the lead plate accounts as it should for missing events, but it does not account for the shift in the  $\pi^0$  direction introduced by our fitting procedure; i.e., a  $\pi^0$  headed just into the hole will be deflected if it emits a  $\gamma$  just out of the hole, but the converse is not true. We conclude that there is no evidence in our data for interference between  $\pi p$  resonances and the  $\rho^-$ .

It is of course best to study the overlap discussed above in an experiment for which the complete range of kinematic variables is observed for all three of the final-state particles of reaction (1). Eisner *et al.*<sup>7</sup> found in such an experiment at 4.2 GeV/c that the cross section for  $\Delta^+(1236)$  is nearly a third of the  $\rho^-$  cross section, but that there is no significant overlap between the  $\rho^-$  and the  $\Delta^+$ .

### VII. DIPION MASS SPECTRUM

We have carried out a detailed study of the dipion mass spectrum for events from reaction (1). Our purpose is to estimate the relative fractions of  $\rho$  resonance and nonresonant background production and the mass and width of the  $\rho$  resonance.

Figure 13 shows the dipion mass spectra we observe for various values of  $t$ . These distributions are limited, for instrumental reasons, to values of  $\omega$  between 0.6 and 1.1 GeV/c<sup>2</sup> and to values of  $t$  between  $-0.35$  and  $-0.04$  (GeV/c)<sup>2</sup>. The lower limits at  $\omega = 0.6$  GeV/c<sup>2</sup> and  $t = -0.35$  (GeV/c)<sup>2</sup> are necessary because of the prescanning cuts (described in Sec. III) at  $\omega^2 = 0.3$  (GeV/c<sup>2</sup>)<sup>2</sup> and  $-t = 0.4$  (GeV/c)<sup>2</sup>. The limits here are tighter than the prescanning cuts to allow for edge effects due to the shifts in  $\omega$  and  $t$  when the complete fit to reaction (1) is carried out. These shifts are simply the measurement errors near the limits in question,  $\Delta\omega \sim 0.04$  GeV/c<sup>2</sup> and  $\Delta t \sim 0.03$  (GeV/c)<sup>2</sup>. An upper limit at  $\omega = 1.1$  GeV/c<sup>2</sup> is placed to avoid having to use events for which the geometrical detection efficiency becomes small. Finally, the upper limit on  $t$  actually depends on  $\omega$ . For  $\omega < 0.8$  GeV/c<sup>2</sup> we observe no events with  $t > -0.04$  because the recoil protons for more positive  $t$  fail to escape from the hydrogen target. For  $\omega \geq 0.85$  GeV/c<sup>2</sup>, the upper limit decreases with increasing  $\omega$  as can be seen from the proton trigger kinematics curves in Fig. 1.

To estimate the amount of  $\rho^-$  production, and the resonance parameters, the spectra have been fitted to the form

$$F(\omega) = Af_{\text{BW}}(\omega)R_1(\omega) + Bf_{\text{BG}}(\omega)R_2(\omega), \quad (5)$$

where  $f_{\text{BW}}(\omega)$  is a Breit-Wigner resonance function,  $f_{\text{BG}}(\omega)$  is three-body phase-space background, and  $R_1(\omega)$  and  $R_2(\omega)$  are functions to take into ac-

count the range of  $t$  available for each value of  $\omega$ . The functions  $R_1(\omega)$  and  $R_2(\omega)$  are given by

$$R_i = \int_{t_{\text{min}}}^{t_{\text{max}}} \exp(B_i t) dt, \quad (6)$$

where  $\exp(B_i t)$  is the shape of the  $t$  distribution at fixed  $\omega$  to be demonstrated in the next section.

We find in the next section that  $B_1 = 9.7$  (GeV/c)<sup>-2</sup> ( $\rho$  production) and  $B_2 = 8.0$  (GeV/c)<sup>-2</sup> (background). The limits  $t_{\text{min}}$  and  $t_{\text{max}}$  are either the fixed limits of cuts or the  $\omega$ -dependent geometrical limit de-

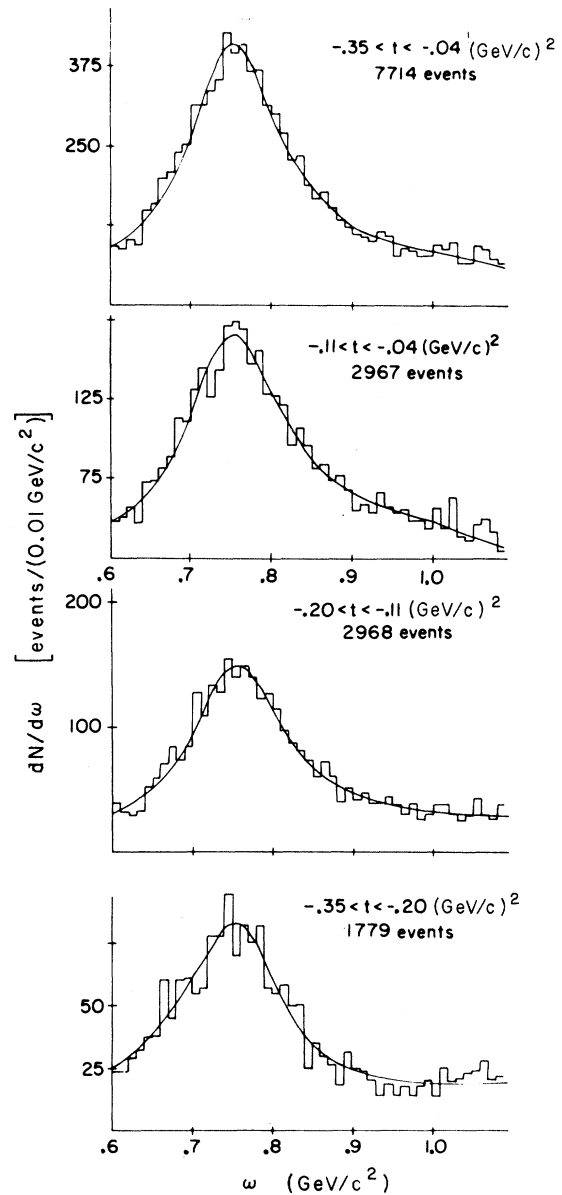


FIG. 13. ( $\pi^-\pi^0$ ) mass spectra for various  $t$  intervals. The smooth curves are fits of the (Breit-Wigner) + (phase-space) form to the data (see the text for details).

scribed above. We remark that  $R_1(\omega)$  and  $R_2(\omega)$  are very slowly varying functions of  $\omega$ . The basic form used for  $f_{\text{BW}}(\omega)$  is

$$f_{\text{BW}}(\omega) = f(\omega) \frac{\omega_r^2 \Gamma^2(\omega)}{(\omega^2 - \omega_r^2)^2 + \omega_r^2 \Gamma^2(\omega)}. \quad (7)$$

We have tried a number of the parametrizations for  $f(\omega)$  and  $\Gamma(\omega)$  used in previous studies of the  $\rho$  mass spectrum.<sup>19</sup> These parametrizations are listed in the first column of Table II. The quantities  $q$  and  $R$  that appear in some of the expressions for  $\Gamma(\omega)$  are, respectively, the pion momentum in the dipion rest frame, and a parameter representing an interaction radius in the scattering.<sup>19</sup>

Table II shows the results of various combinations of  $f(\omega)$  and  $\Gamma(\omega)$  fitted to the data by means of Eqs. (5), (6), and (7). We find that Fit 2, the form used in several lower-energy experiments,<sup>8</sup> does not drop off fast enough with increasing  $\omega$  to give a good fit to the data of this experiment. However, by giving  $f(\omega)$  an  $\omega^{-4}$  dependence, the fit is considerably improved, as in Fit 5. The values for  $R$  in Fit 3 are zero because this value, with the constraint that  $R$  be positive, gives the most rapid falloff with increasing  $\omega$ .

We take Fit 5 as our best fit. The relative fractions of  $\rho$  production (for Fit 5) listed in Table II are used in the next section to calculate the total cross section for  $\rho$  production. The resonance parameters from Fit 5 are  $\omega_r = 766 \pm 4 \text{ MeV}/c^2$  and  $\Gamma_r = 146 \pm 8 \text{ MeV}/c^2$ , where the errors are purely statistical, and the mean measurement error,  $\Delta\omega = 20 \text{ MeV}/c^2$ , has been subtracted in quadrature from the width. These values agree well with present world averages.<sup>20</sup> We should emphasize that the significance of the  $\rho$  parameters determined in this way is not very clear. Some of the difficulties are pointed out in Ref. 20. We will discuss this further in Sec. IX where we show that the mass spectrum for  $\rho^-$  production is much more strongly correlated with the decay configuration than is the spectrum for  $\rho^0$  production. It appears that only by studying the simultaneous production and decay distributions in very-high-statistics experiments can the significance of the resonance parameters be understood.

#### VIII. DIFFERENTIAL CROSS SECTION FOR $\rho$ PRODUCTION

In order to study the  $t$  dependence of the events in various dipion mass intervals, and, in particu-

TABLE II. Fits of various Breit-Wigner forms to the dipion mass spectra. All of  $t$  interval is  $-0.04$  to  $-0.35$   $(\text{GeV}/c)^2$ .  $t$  intervals 1, 2, and 3 are, respectively,  $-0.04 > t > -0.11$ ,  $-0.11 > t > -0.20$ , and  $-0.20 > t > -0.35$   $(\text{GeV}/c)^2$ . Fit 5 is the fit used for calculating the fraction of  $\rho$  production in  $\rho$  region.

Fit	$f(\omega)$	$\Gamma(\omega)$	Degrees of freedom	$t$	$\chi^2$	% $\rho$ 660 to 860	$\omega_r$ (MeV/ $c^2$ )	$\Gamma_r$ (MeV/ $c^2$ )	$A$	$R$ [(GeV/ $c$ ) $^{-1}$ ]
1	1	$\Gamma_r$	46	all	82	82	760	132		
				1	78	86	763	131		
				2	54	81	764	132		
				3	44	80	757	142		
2	1	$\Gamma_r \left(\frac{q}{q_r}\right)^3 \left(\frac{\omega_r}{\omega}\right)$	46	all	144	99	740	159		
				1	81	100	744	146		
				2	70	98	745	156		
				3	80	99	735	173		
3	1	$\Gamma_r \left(\frac{q}{q_r}\right)^3 \left(\frac{\omega_r}{\omega}\right) \left(\frac{1+R^2 q_r^2}{1+R^2 q^2}\right)$	45	all	75	82	759	134		0
				1	72	87	762	134		0
				2	51	82	763	134		0
				3	45	80	756	144		0
4	$\left(\frac{\omega_r}{\omega}\right)^4$	$\Gamma_r$	45			Same as Fit 1; sets $A = 0$				
5	$\left(\frac{\omega_r}{\omega}\right)^4$	$\Gamma_r \left(\frac{q}{q_r}\right)^3 \left(\frac{\omega_r}{\omega}\right)$	45	all	63	85	766	148	3.4	
				1	54	94	762	157	2.3	
				2	45	85	768	148	3.1	
				3	43	78	780	142	6.0	
6	$\left(\frac{\omega_r}{\omega}\right)^4$	$\Gamma_r \left(\frac{q}{q_r}\right)^3 \left(\frac{\omega_r}{\omega}\right) \left(\frac{1+R^2 q_r^2}{1+R^2 q^2}\right)$	44	all	62	84	760	143	1.7	2.3
				1	54	93	760	154	1.7	1.2
				2	44	84	762	144	1.6	2.1
				3	43	78	774	138	4.1	2.6

lar, to calculate the  $\rho$  production cross section, we have made histograms of events vs  $t$  for the mass intervals of interest.

The data for three dipion mass intervals of different widths centered on the  $\rho$  region are shown in Fig. 14. For  $t > -0.10$  ( $\text{GeV}/c^2$ ) we begin to lose events due to the inability of the protons from the far side of the target to reach the proton counter. The differential cross section for the widest mass interval (660–860  $\text{MeV}/c^2$ ) turns out to be nearly the same as the cross section for  $\rho$  production. Using the results of the fits to the dipion mass spectra (Fit 5) to estimate the fraction of  $\rho$  production for various intervals of  $\omega$ , we find that the differential cross section for the widest mass interval needs to be increased by only 9% to be equal to the differential cross section for  $\rho$  production.

The straight lines drawn in Fig. 14 are fits of the form  $A \exp(Bt)$  to the data. Table III gives the values of the parameters for fits to the three distributions shown in Fig. 14 as well as the values of  $B$  for fits to events in a dipion mass interval above and below the  $\rho$  region; the errors in Table III are statistical errors at the 95% confidence

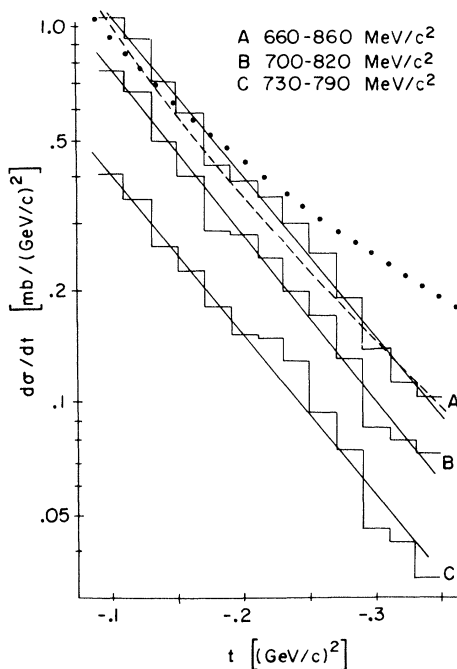


FIG. 14. Differential cross sections for dipion production in various dipion mass intervals centered around the  $\rho$  mass. The straight lines are fits of the  $A \exp(Bt)$  form to the data. The dotted curve is the OPEA prediction for  $\rho$  production taken from calculations of Jackson *et al.*; the dashed curve is the OPEA prediction from the calculations of Oh *et al.*

level. The values  $B_1$  and  $B_2$  used in the preceding section for the  $t$  dependence of the Breit-Wigner and background terms in the fits to the mass spectra are, respectively, the first entry in Table III, and the average of the last two entries. The value of the slope,  $B$ , that we measure for  $\rho^-$  production agrees fairly well with the slope seen in experiments at higher<sup>10</sup> and lower<sup>6</sup> energies.

The dotted curve shown in Fig. 14 is arrived at by taking the OPEA calculation of Jackson *et al.*<sup>21</sup> for 4  $\text{GeV}/c$  and projecting it to 5  $\text{GeV}/c$  assuming a  $1/P_{\text{lab}}^2$  dependence. The dashed curve is the OPEA prediction arrived at by taking the calculation of Oh *et al.*<sup>10</sup> for 7  $\text{GeV}/c$  and projecting it to 5  $\text{GeV}/c$  with the  $1/P_{\text{lab}}^2$  dependence. Oh's calculation follows the Durand and Chiu<sup>13</sup> OPEA formalism and includes the effect of nucleon-pole terms. Jackson's calculations were done when only a small amount of data was available for high  $P_{\text{lab}}$  and larger  $|t|$ ; by varying the final-state absorption, his calculations could probably be brought into satisfactory agreement with our data. We do not take this agreement of our differential cross section with OPEA calculations to mean that one-pion exchange dominates. Instead, it shows the latitude of the OPEA model to fit the production cross sections at larger values of  $|t|$ .

We see only a limited range of  $t$  and therefore cannot directly measure the total cross section for  $\rho^-$  production. However, if we assume  $d\sigma/dt$  has an exponential form for all  $t$  and integrate from  $t=0$  to  $t=-\infty$ , we calculate the total cross section for  $\rho$  production to be 0.31 mb. We know that  $d\sigma/dt$  actually dips for  $t$  near 0 and that the slope becomes less steep for large  $|t|$ . Using our method to compute the total cross section for the experiment of Oh *et al.*<sup>10</sup> and then comparing it to the total cross section they actually measured, we estimate that our above calculation of the total cross section is 10–15% low, giving a total cross section of  $0.35 \pm 0.06$  mb. The error here includes, in addition to the uncertainty in the correction procedure just described, the statistical and normalization uncertainties in our own experiment.

TABLE III. Fits of  $A \exp(Bt)$  form to  $d\sigma/dt$  for dipion production in various mass intervals.

Dipion mass ( $\text{MeV}/c^2$ )	A [ $\text{mb}/(\text{GeV}/c)^2$ ]	B [ $(\text{GeV}/c)^{-2}$ ]	$\chi^2/\text{degrees of freedom}$
660–860	$2.81 \pm 0.30$	$9.73 \pm 0.59$	14.3/11
700–820	$2.10 \pm 0.28$	$10.09 \pm 0.74$	15.2/11
730–790	$1.09 \pm 0.17$	$9.81 \pm 0.88$	12.2/11
450–660		$7.25 \pm 1.70$	19.6/11
860–1100		$8.84 \pm 1.05$	18.2/11

IX.  $\rho^-$  DECAY

It is well known<sup>15</sup> that the decay distributions of an unstable particle are more sensitive to the details of its production mechanism than are the production distributions of the particle. We next discuss our decay angular distributions for  $\rho^- \rightarrow \pi^- + \pi^0$ . Particular emphasis will be placed on the dependence of these angular distributions on di-

pion mass ( $\omega$ ) and production four-momentum transfer squared ( $t$ ).

There is now considerable evidence<sup>22</sup> that for incident  $\pi^-$  momentum up to 3 GeV/c, the decay of the  $\pi^- \pi^0$  system is adequately described by dipion angular momenta of  $l=0$  and  $l=1$ . We assume this to be true in this paper. Angular momentum and parity conservation then lead<sup>23</sup> to the joint production and decay differential cross section

$$\frac{dN}{d\Omega_{\pi\pi}} = N_{(s,t,\omega)} \frac{3}{4\pi} \left[ (2/\sqrt{3}) \text{Re}\rho_{s0} \cos\theta - 2\left(\frac{2}{3}\right)^{1/2} \text{Re}\rho_{s1} \sin\theta \cos\phi + (\rho_{00} + \frac{1}{3}\rho_s) \cos^2\theta + (\rho_{11} + \frac{1}{3}\rho_s) \sin^2\theta - \sqrt{2} \text{Re}\rho_{10} \sin 2\theta \cos\phi - \rho_{1-1} \sin^2\theta \cos 2\phi \right]. \quad (8)$$

The coefficients  $\rho$  are the independent spin-density-matrix elements for the decay and  $N_{(s,t,\omega)} \propto d^2\sigma/dtd\omega^2$  is the number of events per interval of  $t$  and  $\omega^2$ .  $s$  is the square of the total energy in the production center-of-mass system; the angles  $\theta$  and  $\phi$  are standard polar and azimuthal angles of the decay  $\pi^-$  with respect to axes (defined below) in the  $\rho$  rest frame and  $d\Omega_{\pi\pi} = \sin\theta d\theta d\phi$ .

There are two sets of axes with respect to which it is natural to study the decay distributions. To define these reference frames, we denote unit vectors along the beam pion momentum and the recoil proton momentum in the  $\rho$  rest frame by  $\hat{b}$  and  $\hat{r}$ , respectively. Then the first of these frames (Gottfried-Jackson) is defined by  $\hat{Z}_{GJ} = \hat{b}$  and  $\hat{y} = \hat{r} \times \hat{b} / |\hat{r} \times \hat{b}|$ . The second frame (helicity) has the same  $y$  axis, but a  $z$  axis defined by  $\hat{Z}_H = -\hat{r}$ , as illustrated in Fig. 15. We will present our decay angular distributions with respect to both frames since each frame is useful. The Gottfried-Jackson frame has the advantage that  $\rho$  production by pion exchange in the Born approximation gives a pure  $\cos^2\theta_{GJ}$  distribution or  $\rho_{00}^{GJ} = 1$ , with other density-matrix elements equal to zero. The helicity frame is useful in studying the effects of the production mechanism on decay distributions when probability absorption is taken into account; the absorption corrections are applied to amplitudes expressed in the helicity frame and some properties of the Born amplitudes, particularly the dependence on dipion mass and production energy remain as factors after absorption corrections are applied.<sup>24</sup>

In order to determine the density-matrix elements, we first fit the data in a given interval of  $t$  and  $\omega$  to Eq. (8) by the method of least squares. That is, we determine the quantities  $N\rho$  with no normalization constraint on the  $\rho$ 's. The rapid  $t$  and  $\omega$  dependence of  $N(t, \omega)$  is then removed by applying the conventional normalization condition

$$(\rho_{00} + \frac{1}{3}\rho_s) + 2(\rho_{11} + \frac{1}{3}\rho_s) = 1.$$

There is of course no way that the  $\frac{1}{3}\rho_s$  term can be determined separately from the procedure outlined above.

The density-matrix elements obtained in this way are given in Figs. 16 and 17 and Tables IV and V for the helicity and Gottfried-Jackson frames, respectively. The horizontal bars in the figures indicate the  $t$  interval over which the fit was made. The vertical error bars represent statistical uncertainties only (by changing the correcting weight factors one at a time an amount corresponding to the possible systematic error made in each correction and then refitting the data, the effect of systematic errors on the matrix elements was found to be an order of magnitude smaller than the statistical uncertainties). Note that the values of  $\chi^2$  given in Tables IV and V for these fits are satisfactory since there were 100 data points (10 bins each for  $\cos\theta$  and  $\phi$ ) and either four or six parameters. The matrix elements for the mass intervals 660–860 GeV/c<sup>2</sup> were determined with only four parameters since  $\text{Re}\rho_{s0}$  and  $\text{Re}\rho_{s1}$  were set to zero for reasons to be

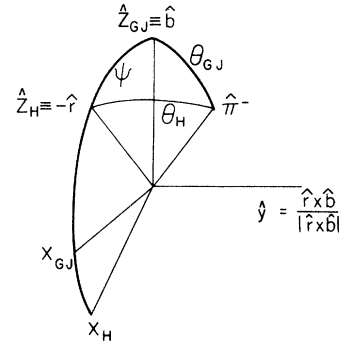


FIG. 15. Orientations of the helicity ( $H$ ) and Gottfried-Jackson ( $GJ$ ) axes in the  $\rho$  rest frame. The unit vectors  $\hat{b}$ ,  $\hat{r}$ , and  $\hat{\pi}^-$  are along the beam pion, recoil proton, and decay  $\pi^-$  momentum, respectively.

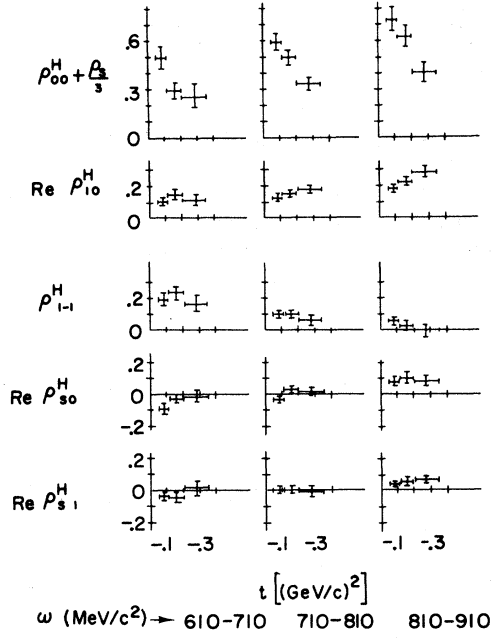


FIG. 16. Density-matrix elements in the helicity frame as a function of dipion mass and  $t$ .

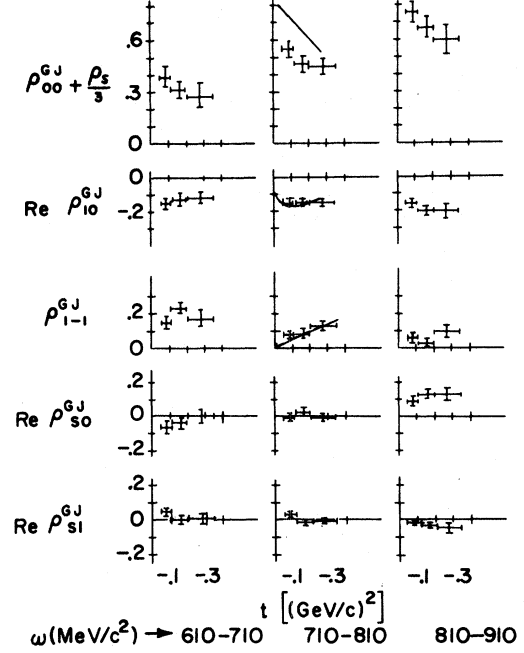


FIG. 17. Density-matrix elements in the Gottfried-Jackson frame as a function of dipion mass and  $t$ . The OPEA predictions for the  $\rho^-$  density-matrix elements are shown as solid curves.

TABLE IV. Density-matrix elements for various intervals of  $t$  and dipion mass in the helicity reference frame.

	$\omega$ (MeV/c <sup>2</sup> )	$t$ intervals [(GeV/c) <sup>2</sup> ]		
		-0.04 to -0.11	-0.11 to -0.20	-0.20 to -0.35
$\rho_{00}^H + \frac{1}{3}\rho_s^H$	660-860	$0.59 \pm 0.03$	$0.47 \pm 0.03$	$0.36 \pm 0.04$
	610-710	$0.50 \pm 0.07$	$0.29 \pm 0.05$	$0.26 \pm 0.07$
	710-810	$0.59 \pm 0.05$	$0.50 \pm 0.04$	$0.33 \pm 0.05$
	810-910	$0.73 \pm 0.07$	$0.63 \pm 0.07$	$0.40 \pm 0.06$
$\text{Re} \rho_{10}^H$	660-860	$0.13 \pm 0.01$	$0.16 \pm 0.02$	$0.18 \pm 0.02$
	610-710	$0.10 \pm 0.03$	$0.14 \pm 0.03$	$0.11 \pm 0.03$
	710-810	$0.12 \pm 0.02$	$0.15 \pm 0.02$	$0.18 \pm 0.02$
	810-910	$0.18 \pm 0.02$	$0.22 \pm 0.03$	$0.28 \pm 0.04$
$\rho_{1-1}^H$	660-860	$0.12 \pm 0.02$	$0.11 \pm 0.02$	$0.08 \pm 0.03$
	610-710	$0.19 \pm 0.04$	$0.23 \pm 0.04$	$0.17 \pm 0.05$
	710-810	$0.10 \pm 0.02$	$0.10 \pm 0.02$	$0.07 \pm 0.03$
	810-910	$0.05 \pm 0.02$	$0.03 \pm 0.03$	$0.00 \pm 0.04$
$\text{Re} \rho_{s0}^H$	610-710	$-0.09 \pm 0.03$	$-0.03 \pm 0.03$	$-0.01 \pm 0.04$
	710-810	$-0.03 \pm 0.02$	$0.03 \pm 0.02$	$0.02 \pm 0.02$
	810-910	$0.09 \pm 0.03$	$0.10 \pm 0.03$	$0.09 \pm 0.03$
$\text{Re} \rho_{s1}^H$	610-710	$-0.02 \pm 0.02$	$-0.02 \pm 0.02$	$0.01 \pm 0.02$
	710-810	$0.003 \pm 0.01$	$0.003 \pm 0.01$	$-0.002 \pm 0.02$
	810-910	$0.035 \pm 0.01$	$0.06 \pm 0.02$	$0.07 \pm 0.02$
$\chi^2$	660-860	105	104	89
	610-710	124	111	129
	710-810	117	110	94
	810-910	92	103	68

described below.

The quality of the least-squares fits can be seen from Figs. 18 and 19 which show the dependence of the dipion angular distributions on  $\cos\theta$  for various  $\phi$  bins in the helicity and Gottfried-Jackson frames, respectively. The solid curves show the fit for the dipion mass interval 660 to 860 MeV/ $c^2$  with  $\text{Re}\rho_{s0}$  and  $\text{Re}\rho_{s1}$  constrained to be zero. Figures 18 and 19 also show clearly the strong correlation between  $\cos\theta$  and  $\phi$  already evident from the nonzero values of  $\text{Re}\rho_{10}$  and  $\rho_{1-1}$ .

We now outline the main features of our results. Each of these features will then be discussed in detail.

(1) Interference between  $s$ - and  $p$ -wave terms in the dipion angular distribution is small. This is indicated by the small values of  $\rho_{s0}$  and  $\rho_{s1}$  relative to the dominant  $l=1$  elements,  $\rho_{00} + \frac{1}{3}\rho_s$ ,  $\text{Re}\rho_{10}$ , and  $\rho_{1-1}$ . The values of  $\rho_{s0}$  and  $\rho_{s1}$  in the  $\rho$  region  $\omega = 710\text{--}810$  MeV/ $c^2$  are consistent with no interference at all.

(2) The  $l=1$  density-matrix elements depend strongly on dipion mass in the mass region  $610 < \omega < 910$  MeV/ $c^2$ . In the helicity frame,  $\rho_{00} + \frac{1}{3}\rho_s$  and  $\text{Re}\rho_{10}$  increase rapidly with increasing  $\omega$  while  $\rho_{1-1}$  decreases rapidly with increasing  $\omega$ . This behavior of  $\rho_{1-1}$  has been observed at lower energies ( $\sim 2.5$  GeV) and has been interpreted as evi-

dence that  $\omega^0$  exchange may contribute significantly to  $\rho^-$  production even at low energy.<sup>11</sup>

(3) The density-matrix elements in the  $\rho^-$  mass region  $710 < \omega < 810$  MeV/ $c^2$  are not consistent with OPEA predictions (or with the density-matrix elements from  $\rho^0$  production experiments). The solid curves in Fig. 17 are the OPEA predictions as calculated by Eisner *et al.*<sup>7</sup> for 4.2 GeV/ $c$  incident  $\pi^-$ . The large difference between the experimental value of  $\rho_{00}$  and OPEA predictions has been noted previously<sup>7,9,10</sup> and has been attributed to  $\omega^0$  exchange.

The rest of this section will be divided into two parts. First, we discuss the interference terms. One result of this discussion is an estimate of  $\rho_s$  which in turn allows us to find  $\rho_{00}$  and  $\rho_{11}$  [see Eq. (8)]. Second, we discuss the details of the mass and  $t$  dependence of the density-matrix elements and the implications of these dependences for the exchange mechanism in  $\rho^-$  production.

#### 1. Interference Between $s$ - and $p$ -Wave Terms

The  $s$ - $p$  interference terms have recently been used by several groups<sup>8,10</sup> to determine the  $s$ -wave phase shift for  $\pi^-\pi^0$  scattering on the mass shell. The  $\pi^-\pi^0$  angular distribution on the mass shell in the Gottfried-Jackson frame is<sup>23</sup>

TABLE V. Density-matrix elements for various intervals of  $t$  and dipion mass in the Gottfried-Jackson reference frame.

	$\omega$ (MeV/ $c^2$ )	$t$ interval [(GeV/ $c$ ) <sup>2</sup> ]		
		-0.04 to -0.11	-0.11 to -0.02	-0.20 to -0.35
$\rho_{00}^{\text{GJ}} + \frac{1}{3}\rho_s$	660-860	0.58 ± 0.03	0.48 ± 0.03	0.42 ± 0.04
	610-710	0.39 ± 0.06	0.32 ± 0.05	0.28 ± 0.07
	710-810	0.55 ± 0.04	0.46 ± 0.05	0.45 ± 0.05
	810-910	0.76 ± 0.07	0.67 ± 0.06	0.60 ± 0.08
$\text{Re}\rho_{10}^{\text{GJ}}$	660-860	-0.16 ± 0.01	-0.16 ± 0.02	-0.15 ± 0.02
	610-710	-0.17 ± 0.03	-0.12 ± 0.03	-0.11 ± 0.03
	710-810	-0.16 ± 0.02	-0.16 ± 0.02	-0.15 ± 0.02
	810-910	-0.16 ± 0.02	-0.20 ± 0.03	-0.20 ± 0.04
$\rho_{1-1}^{\text{GJ}}$	660-860	0.09 ± 0.02	0.11 ± 0.02	0.14 ± 0.03
	610-710	0.16 ± 0.04	0.23 ± 0.04	0.18 ± 0.06
	710-810	0.08 ± 0.02	0.09 ± 0.03	0.13 ± 0.03
	810-910	0.06 ± 0.02	0.03 ± 0.03	0.10 ± 0.04
$\text{Re}\rho_{s0}^{\text{GJ}}$	610-710	-0.07 ± 0.03	-0.04 ± 0.03	0.004 ± 0.04
	710-810	-0.01 ± 0.02	0.02 ± 0.02	-0.01 ± 0.02
	810-910	0.09 ± 0.03	0.13 ± 0.03	0.12 ± 0.04
$\text{Re}\rho_{s1}^{\text{GJ}}$	610-710	0.04 ± 0.02	0.006 ± 0.02	0.006 ± 0.02
	710-810	0.02 ± 0.01	-0.01 ± 0.01	-0.006 ± 0.01
	810-910	-0.01 ± 0.01	-0.02 ± 0.01	-0.03 ± 0.02
$\chi^2$	660-860	104	109	87
	610-710	150	114	139
	710-810	95	165	67
	810-910	89	92	82

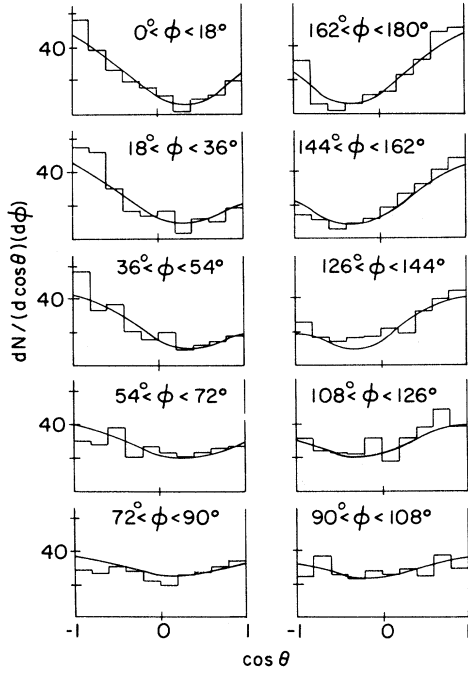


FIG. 18. Simultaneous  $\cos\theta$  and  $\phi$  distribution for  $-0.04 > t > -0.35$  ( $\text{GeV}/c^2$ ) and  $660 < \omega < 860$   $\text{MeV}/c^2$  in the helicity frame. The smooth curves are the fit of Eq. (8) to the data with  $\text{Re}\rho_{s_0} = \text{Re}\rho_{s_1} = 0$ .

$$\frac{d\sigma}{d\Omega_{\pi\pi}} = \frac{1}{q^2} [\sin^2\delta_0^2 + 6 \cos(\delta_0^2 - \delta_1^1) \sin\delta_0^2 \sin\delta_1^1 \cos\theta + 9 \sin^2\delta_1^1 \cos^2\theta]. \quad (9)$$

The superscripts on the phase shifts,  $\delta$ , label the isotopic spin and the subscripts label the orbital angular momentum;  $q$  is the pion momentum in the dipion rest frame. In order to isolate the interference term [coefficient of  $\cos\theta$  in Eq. (9)], it is convenient to study the asymmetry ratio  $(F - B)/(F + B)$ , where  $F$  and  $B$  are the numbers of events with  $\cos\theta$  greater than and less than zero, respectively. The asymmetry ratio is related to  $\text{Re}\rho_{s_0}$  and to the phase shifts through

$$\frac{F - B}{F + B} = \sqrt{3} \text{Re}\rho_{s_0} = \frac{3 \cos(\delta_0^2 - \delta_1^1) \sin\delta_0^2 \sin\delta_1^1}{\sin^2\delta_0^2 + 3 \sin^2\delta_1^1}. \quad (10)$$

Baton and Laurens find<sup>8</sup> that the asymmetry ratio is almost independent of  $t$  throughout the physical region  $t > -0.3$  and on the mass shell. We examine the dependence of our asymmetry ratios on  $t$  and on  $\omega$  in Fig. 20, both for the Gottfried-Jackson and helicity frames. We also find no significant  $t$  dependence over our range of ob-

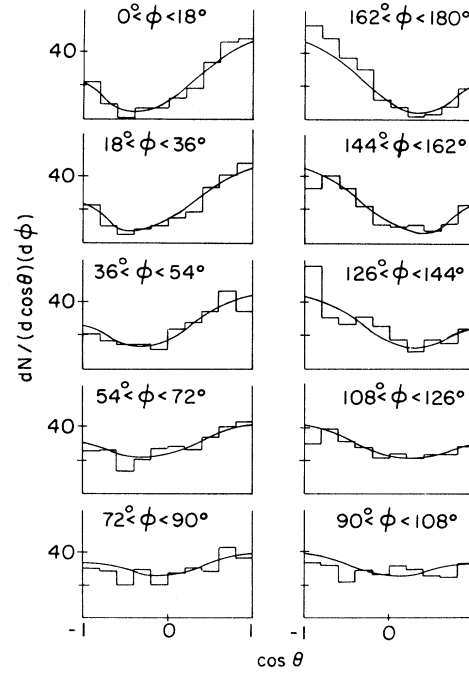


FIG. 19. Simultaneous  $\cos\theta$  and  $\phi$  distribution for  $-0.04 > t > -0.35$  ( $\text{GeV}/c^2$ ) and  $660 < \omega < 860$   $\text{MeV}/c^2$  in the Gottfried-Jackson frame. The smooth curves are the fit of Eq. (8) to the data with  $\text{Re}\rho_{s_0} = \text{Re}\rho_{s_1} = 0$ .

servation.

While the  $\omega$  dependence of our asymmetry ratios is qualitatively similar to that observed<sup>8</sup> by Baton and Laurens, our asymmetries are smaller both below and above the  $\rho$  region, as can be seen by comparing our data with the solid curve in Fig. 20. This curve has been calculated from the on-mass-shell phase shifts of Baton and Laurens, but it gives a good representation of the Baton and Laurens data in the physical region  $t > -0.30$  ( $\text{GeV}/c^2$ ). To pursue this apparent disagreement further, we have collected in Table VI all of the accurate information on  $\rho^-$  interference that we know of. The top part of Table VI gives values of

$$\rho_{s_0} = \frac{1}{\sqrt{3}} \frac{F - B}{F + B}$$

in the Gottfried-Jackson frame, while the bottom part gives the interference density-matrix elements in the helicity frame from a number of bubble-chamber experiments as compiled by Malamud and Schlein.<sup>11</sup> We have not rotated these helicity elements into the Gottfried-Jackson frame because a  $t$  binning of the data is not available to us. However, from the size of the rotation coefficients involved and from the behavior of our own

elements under rotation, we believe that the  $\text{Re}\rho_{s0}$  element would be essentially the same in the Gottfried-Jackson frame. We draw the following conclusions from the data in Table VI: (a) There is no significant dependence of  $\rho_{s0}$  on projectile momentum. This point is germane to the question of dipion production by  $\omega^0$  (or other) exchanges, which might be expected (see Sec. IX 2 below) to play an increasingly important role as projectile momentum increases. (b) Our values of  $\text{Re}\rho_{s0}$  for  $\omega < 810 \text{ MeV}/c^2$  are in good agreement with the weighted average of all of the values given at the bottom of Table VI (we include the values of Malamud and Schlein in the helicity frame in this average, but not, of course, our data listed under the helicity frame). Our value for  $\text{Re}\rho_{s0}$  in the mass bin  $810 \leq \omega \leq 910 \text{ MeV}/c^2$  is about 4 standard deviations lower than the average. We have not been able to find an instrumental source for this difference. (c) The weighted average values of  $\rho_{s0}$  are somewhat smaller than the values of Baton and Laurens.<sup>8</sup> If this average is correct, and the  $\delta_1^1$  ( $\rho$  resonance) phase shift is unchanged, the  $\delta_0^2$  phase shift must be reduced from  $\approx -11^\circ$  to  $\approx -8^\circ$  at the  $\rho$  resonance.

As a final point concerning the interference terms, we note that the  $\rho_s$  density-matrix element should be small compared with  $\rho_{00}$  and  $\rho_{11}$  for  $\pi^-\pi^0$  in the  $\rho$  mass region. The element  $\rho_s$  is related to the phase shifts by

$$\rho_s = (\sin^2 \delta_0^2) / (\sin^2 \delta_0^2 + 3 \sin^2 \delta_1^1).$$

Using the on-mass-shell phase shifts of Baton and Laurens, we find  $\rho_s < 0.06$  throughout the  $\omega$  region 610 to 910  $\text{MeV}/c^2$ . In the rest of this paper we assume that this result applies to the physical region, and in discussions of the elements  $\rho_{00}$  and  $\rho_{11}$ , we neglect the  $s$ -wave contribution.

## 2. Mass and $t$ Dependence of the Density-Matrix Elements

It was pointed out in the Introduction that  $\rho^0$  production and decay are described well by the OPEA model while  $\rho^-$  production is not, and that this situation is perhaps natural since  $\omega^0$  exchange can contribute to  $\rho^-$  production but not to  $\rho^0$  production. In this section we first give empirical evidence that the partial cross sections  $N\rho_{00}^H$  and  $N\text{Re}\rho_{10}^H$  for  $\rho^-$  are consistent with OPEA, while the  $N\rho_{11}^H$  and  $N\text{Re}\rho_{1-1}^H$  are not. We will discuss this result in the context of a model in which  $\pi^0$  and  $\omega^0$  exchanges dominate  $\rho^-$  production.

One would like to test for the effects of nonpionic exchanges by making absolute comparisons of the differential cross sections for  $\rho^0$  and  $\rho^-$  at the same production energy. From charge indepen-

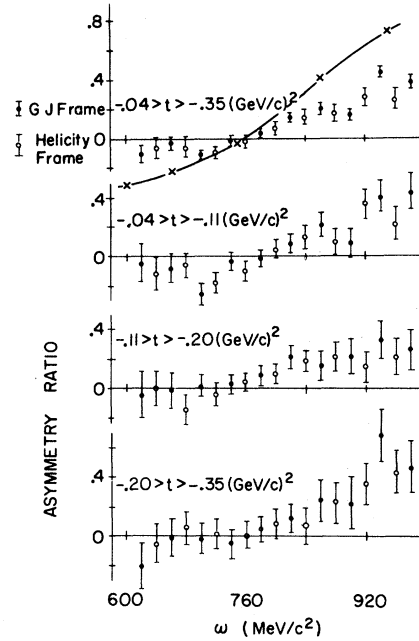


FIG. 20. Forward-backward decay asymmetry as a function of dipion mass for various  $t$  intervals in the Gottfried-Jackson and helicity frames. The mass bins are  $40 \text{ MeV}/c^2$  wide for each frame. The bin centers for the two frames are displaced by  $20 \text{ MeV}/c^2$  for clarity.

dence, all  $\rho^0$  cross sections should be twice as big as the corresponding  $\rho^-$  cross sections if  $\pi$  exchange dominates (see Ref. 10 for a comparison of this type with relatively low statistics data). While we are not able to make such an absolute comparison, we can compare the  $\omega$  dependence of the cross sections for  $\rho^0$  and  $\rho^-$  production. In Fig. 21 we show the  $\omega$  dependence of our partial cross sections  $N\rho^H$  and the cross sections for  $\rho^0$  and  $\rho^-$  production at  $\sim 2.5 \text{ GeV}/c$  incident  $\pi^-$  momentum. The  $2.5\text{-GeV}/c$  data came from a compilation<sup>11</sup> of bubble-chamber results at a number of momenta between 2 and 3  $\text{GeV}/c$  (our procedure for extracting the density-matrix elements from the data of Ref. 11 is described in Appendix B). The cross sections are normalized in each case to give the same total value of  $N\rho_{00}^H$  when summed over the  $\omega$  bins.

This comparison strongly suggests, for reasons outlined below, that the partial cross sections  $N\rho_{00}^H$  and  $N\text{Re}\rho_{10}^H$  for  $\rho^-$  production are consistent with OPEA predictions, at least up to  $5 \text{ GeV}/c$ . We note that (i) the  $\rho^0$  density-matrix elements at  $2.5 \text{ GeV}/c$ ,<sup>11</sup> and  $2.7$  and  $4.1 \text{ GeV}/c$ ,<sup>25</sup> are about the same as those from the recent high-statistics SLAC results<sup>14</sup> at  $15 \text{ GeV}/c$ . Thus the  $\rho^0$  density-matrix elements are consistent with being independent of incident  $\pi^-$  momentum. (ii) Production

TABLE VI. Asymmetry density-matrix element  $\text{Re}\rho_{s0}$  (and  $\text{Re}\rho_{s1}$  when available) for  $\rho^-$  production in  $\pi^-p \rightarrow \pi^-\pi^0p$  at a variety of incident  $\pi^-$  momenta. The bottom entry is, as explained in the text, the weighted average of all the values in the table including the values of Malamud and Schlein in the helicity frame (but not the value from this experiment in the helicity frame).

$P_{\text{lab}}$ (GeV/c)	Source	Ref.	$t$	$\omega$	$\rho_{s0}$	$\rho_{s1}$
Gottfried-Jackson frame						
	Phase shift	8	$+m_\pi^2$	610-710	-0.115	
				710-810	0.012	
				810-910	0.230	
2.77	Baton and Laurens	8	-0.02 to -0.26	610-710	-0.093 ± 0.02	
				710-810	0.017 ± 0.013	
				810-910	0.230 ± 0.015	
4.16	Eisner <i>et al.</i>	7	>-0.30	610-710	+0.05 ± 0.06	
				710-810	-0.01 ± 0.04	
				810-910	0.17 ± 0.05	
5.0	This expt.		-0.04 to -0.275	610-710	-0.047 ± 0.02	
				710-810	0.002 ± 0.013	
				810-910	0.111 ± 0.02	
7.0	Oh <i>et al.</i>	10	>-0.30	610-710	-0.08 ± 0.08	
				710-810	-0.08 ± 0.05	
				810-910	0.15 ± 0.06	
Helicity frame						
2.14 to 3.0	Malamud and Schlein	11	>-0.16	610-710	-0.02 ± 0.02	-0.01 ± 0.01
				710-810	0.04 ± 0.03	0.01 ± 0.01
				810-910	0.20 ± 0.03	0.06 ± 0.01
5.0	This expt.		-0.04 to -0.20	610-710	-0.06 ± 0.02	-0.02 ± 0.02
				710-810	0.00 ± 0.02	0.00 ± 0.01
				810-910	0.10 ± 0.02	0.05 ± 0.01
	Weighted average			610-710	-0.05 ± 0.01	
				710-810	0.006 ± 0.01	
				810-910	0.188 ± 0.01	

and decay of  $\rho^0$  is very well described by OPEA up to 15 GeV/c.<sup>10,14</sup> (iii) The cross sections  $N\rho_{00}^H$  and  $N\text{Re}\rho_{10}^H$  for  $\rho^-$  at 2.5 and at 5.0 GeV/c have the same  $\omega$  dependence (see Fig. 21) as do the corresponding  $\rho^0$  cross sections. It should be emphasized that the ratio  $N\text{Re}\rho_{10}^H/N\rho_{00}^H$  for the 2.5 GeV/c data is the same for  $\rho^-$  and  $\rho^0$ , independent of the normalization procedure used here. The fact that this ratio is the same for our 5-GeV/c  $\rho^-$  data could be fortuitous since the density-matrix elements depend on  $t$  and our data are instrumentally limited to  $t < -0.05$ . We find, however, by integrating the partial cross sections determined from  $\rho^0$  data at 4.1 GeV/c<sup>25</sup> over the  $t$  acceptance of our apparatus, that the relative values of the  $\rho^0$  cross sections shown in Fig. 21 are appropriate to compare with our  $\rho^-$  data.

It is clear from Fig. 21 that the cross sections  $N\rho_{11}^H$  and  $N\rho_{1-1}^H$  are not consistent with OPEA. First, these cross sections are larger (relative to  $N\rho_{00}^H$ ) than their counterparts for  $\rho^0$ . Second,

they have a factor that decreases with increasing  $\omega$  superimposed on the resonant  $\omega$  dependence, while  $N\rho_{00}^H$  and  $N\text{Re}\rho_{10}^H$  have a factor that increases with increasing  $\omega$  superimposed on the resonant  $\omega$  dependence.

The  $t$  dependence of the cross sections  $N\rho_{00}^H$  and  $N\text{Re}\rho_{10}^H$  for  $\rho^-$  production should also be sensitive to the presence of exchanges other than  $\pi$  exchange. We are, unfortunately, not able to compare our cross sections with  $\rho^0$  cross sections over a wide enough  $t$  region to be useful. Our  $t$  dependence is biased for  $t > -0.1$  because some of the recoil protons are not able to escape from the hydrogen target. The  $t$  dependences of the normalized density-matrix elements are, of course, free from this bias since there is no correlation between the probability that a proton does not escape and the decay characteristics of an event (recall from Fig. 1 that all protons exit the hydrogen target at essentially the same lab angle). It is, however, meaningless to compare normalized density-ma-

trix elements for  $\rho^-$  and  $\rho^0$  since the normalization condition  $N\rho_{00} + 2N\rho_{11} = N$  injects the  $t$  dependence of  $N\rho_{11}$  into all of the normalized density-matrix elements. The only useful comparison available is then the ratio  $(\text{Re}\rho_{10}^H)/\rho_{00}^H$ . This will be the same for  $\rho^-$  and  $\rho^0$  if these elements are dominated by  $\pi$  exchange. Figure 22 shows a comparison of our  $\rho^-$  values for this ratio with  $\rho^0$  values from the recent high statistics SLAC<sup>14</sup> data at 15 GeV/c; the two sets of data agree well, at least out to  $-t = 0.2$  (GeV/c)<sup>2</sup>. In summary, comparison of  $\rho^-$  and  $\rho^0$  data shows that the  $\rho^-$  cross sections  $N\rho_{00}^H$  and  $N\text{Re}\rho_{10}^H$  are consistent with pure OPEA for  $t > -0.2$  and  $P_{\text{lab}} \leq 5$  GeV/c, while  $N\rho_{11}^H$  and  $N\rho_{1-1}^H$  increase more rapidly with increasing  $s$  than is required by OPEA and decrease with increasing  $\omega$  unlike OPEA cross sections. We will next compare these results with what is expected if  $\omega^0$  exchange is assumed to be responsible for the deviations of  $\rho^-$  cross sections from OPEA behavior.

To interpret our data, we will first consider the partial cross sections,  $N\rho^H$ , that result from assuming elementary particle  $\pi$  and  $\omega^0$  exchange in the Born approximation. While this is certainly

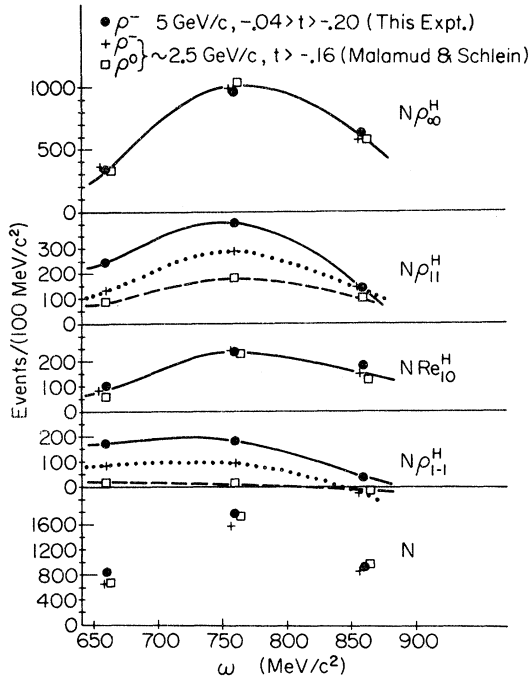


FIG. 21. Dependence of the partial cross sections ( $N\rho^H$ ) on dipion mass ( $\omega$ ) for  $\pi^-p \rightarrow \rho^-p$  at 5 GeV/c and  $\pi^-p \rightarrow \rho^-\rho$  and  $\rho^0n$  at  $\sim 2.5$  GeV/c. The 2.5 GeV/c data are taken from Ref. 11. The curves are drawn free-hand to help the eye to connect data points. Only one curve is drawn when the data points are consistent within statistical uncertainties. These uncertainties are never larger than the data point symbols.

not a realistic model, we are motivated to use it by consideration of the dependence on  $\rho$  mass of the Born amplitudes for  $\pi$  exchange. We will show that this mass dependence gives at least qualitatively the  $\omega$  variation that must be superimposed on a symmetric resonance shape to describe the partial cross sections  $N\rho^H$  for  $\rho^0$  production. It is then of interest to see if  $\omega^0$ -exchange amplitudes can qualitatively explain the  $\omega$  dependence of  $N\rho_{11}^H$  and  $N\rho_{1-1}^H$  for  $\rho^-$  production.

We have calculated, as outlined in Appendix A, the cross sections that follow from the Feynman diagram of Fig. 23. Since we are interested primarily in the  $\omega$  dependence of the dominant amplitudes at 5 GeV/c, we work with the high-energy limits of the elementary-particle-exchange amplitudes. The cross sections that result from expanding each helicity amplitude in powers of  $s^{-1}$  and retaining only the lowest power in  $s^{-1}$  associated with each exchange ( $s^0$  for  $\pi^0$  exchange and  $s^1$  for  $\omega^0$  exchange) are

$$\begin{aligned} N\rho_{00}^H &= 2|K_P|^2\rho^2(1+2t/\rho^2)(-t), \\ N\text{Re}\rho_{10}^H &= 2\sqrt{2}|K_P|^2\rho(1+t/\rho^2)(-t)^{3/2}, \\ N\rho_{1-1}^H &= -4|K_P|^2(-t)^2 + |F_V|^2\rho^{-2}s^2(-t), \\ N\rho_{11}^H &= 4|K_P|^2(-t)^2 + |F_V|^2\rho^{-2}s^2(-t). \end{aligned} \quad (11)$$

The constants  $\rho$ ,  $\pi$ , and  $\omega^0$  represent the stable  $\rho$ ,  $\pi$ , and  $\omega^0$  masses.  $K_P$  and  $F_V$  characterize pseudo-scalar ( $\pi$ ) and vector ( $\omega^0$ ) exchange, respectively, and are related to the coupling constants  $f$  at the meson vertex and  $G$  at the nucleon vertex of the diagram in Fig. 23 by

$$\begin{aligned} |K_P|^2 &= D|i f_{PPV} G_{BBP}(\pi^2 - t)^{-1}|^2, \\ |F_V|^2 &= D|i f_{PVV} G_{BBV}(\omega^0{}^2 - t)^{-1}|^2 \\ &\times \left[ 1 + \left( \frac{G_{BBV}^T}{2NG_{BBV}} \right)^2 (-t) \right]. \end{aligned} \quad (12)$$

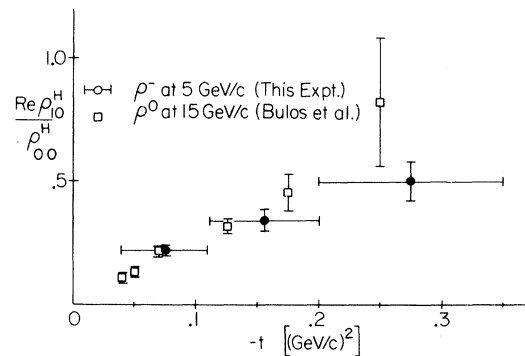


FIG. 22. Dependence of the ratio  $(\text{Re}\rho_{10}^H)/\rho_{00}^H$  on  $t$  for  $\rho^-$  at 5 GeV/c and  $\rho^0$  at 15 GeV/c. The 15 GeV/c data are taken from Ref. 14.

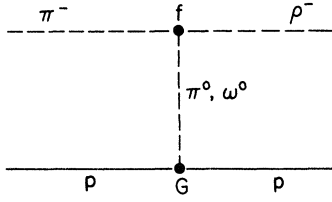


FIG. 23. Feynman diagram for the production of a stable  $\rho^-$  by exchange of  $\pi^0$  or  $\omega^0$ .

The factor  $D$  contains the effects of  $\rho$  decay dynamics and phase space common to all the cross sections;  $G_{BBV}^V$  and  $G_{BBV}^T$  are the independent vector and tensor couplings<sup>26</sup> of  $\omega^0$  at the nucleon vertex.

Before comparing this result with our data, it may be helpful to consider these features of Eq. (11) that can be understood from elementary arguments. We first note that there is no coupling between pseudoscalar and vector exchange; that is, no cross terms involving products of  $\pi$  and  $\omega^0$  exchange amplitudes appear. The cross sections are then sums of the separate cross sections for pure  $\pi$  and  $\omega^0$  exchange. It is easy to see that this must be so from the familiar<sup>15</sup> values of the elementary particle density-matrix elements in the Gottfried-Jackson frame. Angular momentum and parity conservation at the  $\omega\pi\rho$  vertex require that only magnetic substates of the  $\rho$  with  $M=0$  be populated for  $\pi$  exchange and only substates with  $M=\pm 1$  be populated for  $\omega^0$  exchange. Thus the decay distribution is characterized by pure  $\rho_{00}^{GJ}$  for  $\pi$  exchange and a mixture of  $\rho_{11}^{GJ}$  and  $\rho_{1-1}^{GJ}$  for  $\omega^0$  exchange. The absence of interference between  $\pi$  and  $\omega^0$  exchange in the Gottfried-Jackson frame must be preserved by the rotation into the helicity frame since this rotation is purely kinematic. It is somewhat mysterious in the context of this discussion why pseudoscalar terms appear in all four of the  $N\rho^H$  of Eq. (11) by rotation from  $\rho_{00}^{GJ}=1$ , while vector terms do not appear in  $N\text{Re}\rho_{10}^H$  and  $N\rho_{00}$  due to the same rotation. That this happens is a result of the special circumstance that  $\rho_{11}=\rho_{1-1}$  in each frame in the high-energy limit, and the particular form of the rotation coefficients (see Appendix C).

We next compare the dependence of the Born cross sections on dipion mass with the data. For this purpose, we replace the stable  $\rho$  mass,  $\rho$ , in Eq. (11) by the variable dipion mass  $\omega$ , and imagine that this mass factor multiplies a resonance form (contained in the factor  $D$  defined above) that is symmetric about  $\rho$ . One then sees that the  $\omega$  dependence of all of the cross sections of Eq. (11) are in qualitative agreement with the experimental data of Fig. 21. Moreover, the  $\omega$  asymmetries of all four  $\pi$ -exchange cross sections of Fig. 21

( $\rho^0$  cross sections) are quantitatively consistent (within errors) with the  $\omega$  asymmetries of the  $K\rho$  terms of Eq. (11).

The significance of this agreement is certainly not transparent. The factors  $\rho^2$  and  $\rho$  in the first two of Eqs. (11) can be traced to the  $\pi\pi\rho$  vertex in the  $\pi$ -exchange diagram of Fig. 23. They result from a kinematic (angular momentum) effect when two pions react with small momentum transfer through a helicity-0 state of the  $\rho$ . The  $\rho^{-2}$  factors in the last two of Eqs. (11), however, have no dynamical significance. They come from an overall  $\rho^{-1}$  factor inserted in the Born amplitude for dimensional reasons. We have not been able to explain this " $\rho^{-2}$  dependence" of  $N\rho_{11}$  and  $N\rho_{1-1}$  in terms of conventional ideas about the effects of absorption or vertex form factors.<sup>27</sup> Thus we find that the Born amplitudes "explain" the  $\omega$  dependence of the  $\pi$ -exchange cross sections, but do not explain the  $\omega$  dependence of the additional contributions to the  $\rho^-$  cross sections. We regard this circumstance as a deficiency in our description of  $\omega^0$  exchange rather than evidence against an  $\omega^0$ -exchange interpretation of these additional cross sections. Indeed, we will show in the remainder of this section that the relative values of the various  $\rho^-$  partial cross sections near the  $\rho$  mass are consistent with an  $\omega^0$ -exchange interpretation.

We wish to show that it is reasonable that  $\omega^0$  exchange does not contribute to the  $\rho^-$  cross sections  $N\rho_{00}^H$  and  $N\text{Re}\rho_{10}^H$ , and that  $\omega^0$  exchange adds equal amounts to the  $\rho^-$  cross sections  $N\rho_{11}^H$  and  $N\rho_{1-1}^H$  as shown in Fig. 21. It can be seen from Eq. (11) that these properties are true for the elementary particle cross sections, but it is not at all obvious that they remain true when absorption effects are included. A complete quantitative demonstration that absorption effects do not alter these expectations for  $\omega^0$  exchange is rather involved. We therefore rely here on a qualitative and somewhat overstated argument so that the point is clear.

$\rho$  production is described by 12 amplitudes  $M_{\lambda'\lambda}^\mu$ , where  $\mu$  is the  $\rho$  helicity and  $\lambda'$  is the final nucleon helicity. Invariance under reflection through the production plane reduces the number of independent amplitudes to six, which we take to be  $M_{++}^\mu$  and  $M_{+-}^\mu$ . We assume that only  $\pi$ -exchange amplitudes,  $P$ , and  $\omega^0$ -exchange amplitudes,  $V$ , are important so that

$$M_{\lambda'\lambda}^\mu = P_{\lambda'\lambda}^\mu + V_{\lambda'\lambda}^\mu. \quad (13)$$

In the high-energy limit,  $s \gg 1$ , many of the remaining 12 amplitudes are of higher order in  $s^{-1}$  than the dominant amplitudes, so they may be dropped. From the energy dependences of the Born amplitudes in Eq. (A9) (Appendix A) we find that the surviving amplitudes are

$$P_{+-}^0, P_{+-}^1, P_{+-}^{-1}, V_{++}^1, V_{++}^{-1}, V_{+-}^1, \text{ and } V_{+-}^{-1}. \quad (14)$$

As we will show, our data are consistent with the supposition that the last two of the  $\omega^0$  amplitudes are small compared with the first two. There is some evidence that this should be so.  $V_{+-}^1$  and  $V_{+-}^{-1}$  are proportional to  $G_{BBV}^T$  [defined above in Eq. (12)] while  $V_{++}^1$  and  $V_{++}^{-1}$  are proportional to  $G_{BBV}^V$ . Jackson *et al.* have suggested that one might expect  $G^T/G^V \ll 1$  in analogy with results from analysis of electromagnetic form factors.<sup>21</sup> Yen *et al.*<sup>28</sup> have found a preferred value of zero for  $G^T/G^V$  in an absorption model fitted to about 1000  $\rho^-$  events at 4.16 GeV/c. Finally, Kane *et al.*<sup>29</sup> find  $G^T/G^V = 0.5$  from a Regge-pole plus absorptive-cut analysis of many reactions (particularly photoproduction of pions). If we accept the value  $G^T/G^V = 0.5$  for the sake of argument, we find that  $V_{+-}^1$  and  $V_{+-}^{-1}$  are suppressed relative to  $V_{++}^1$  and  $V_{++}^{-1}$  by a factor  $\alpha$  given by

$$\alpha \sim (G^T/2NG^V)\sqrt{-t} \sim 0.1 \quad (15)$$

for the  $t$  range of our experiment.

It is clear from the list (14) of dominant amplitudes that  $\omega^0$  exchange should not contribute significantly to  $N\rho_{00}^H$  since this cross section contains only terms of the form  $|M_{\lambda',\lambda}^0|^2$ . This result agrees with the first of our observations concerning the data of Fig. 21. The remaining observations are tested by substituting the list (14), omitting the last two amplitudes because of (15), into Eqs. (A11) for the partial cross sections. We find (suppressing the normalization of all cross sections to the same  $N\rho_{00}^H$ )

$$\begin{aligned} N \operatorname{Re} \rho_{10}^H(\rho^-) - N \operatorname{Re} \rho_{10}^H(\rho^0) &= 0, \\ N\rho_{11}^H(\rho^-) - N\rho_{11}^H(\rho^0) &= |V_{++}^1|^2 + |V_{++}^{-1}|^2, \\ N\rho_{1-1}^H(\rho^-) - N\rho_{1-1}^H(\rho^0) &= 2 \operatorname{Re} V_{++}^1 V_{++}^{-1*}. \end{aligned} \quad (16)$$

The final point in our argument is that the absorption correction to a  $t$ -channel amplitude at high energy depends on helicities only through the net helicity flip  $n = |\mu + \lambda - \lambda'|$ .<sup>30</sup> The two  $t$ -channel-exchange amplitudes are equal<sup>30</sup> [this is also shown by explicit calculation in Eqs. (A9)], and since each amplitude has  $n=1$ , the two amplitudes are absorbed equally. As a result  $V_{++}^1 = V_{++}^{-1}$  even after absorption effects, and the right-hand sides of the last two of Eqs. (16) are equal. Before summarizing the results of this discussion, we remark that we have carried out quantitative calculations of the effects of absorption using the method of Henyey, Kane, Pumplin, and Ross, and the parameters given in Ref. 29. We find that for  $G^T/G^V \leq 0.5$ , the deviations from Eqs. (16) are not more than the statistical errors of the data of Fig.

21, which are about the size of the data symbols.

In conclusion, we believe that our data in the  $\rho$  region  $710 \leq \omega \leq 810$  MeV/c<sup>2</sup> are consistent with present understanding of  $\pi$  and  $\omega^0$  exchanges. The discussion of absorbed  $\pi$  and  $\omega^0$  exchange given above suggests that: (1) the  $\omega^0$ -exchange contribution to the  $\rho^-$  cross section can be described well by a single amplitude ( $V_{++}^1$ ); (2) there is no significant interference between  $\pi$  and  $\omega^0$  exchange amplitudes; (3) only  $N\rho_{11}^H$  and  $N\rho_{1-1}^H$  receive  $\omega^0$ -exchange contributions and these contributions are equal. Our data are consistent with these results. The  $\omega^0$ -exchange cross sections found by subtracting the  $\rho^0$  cross sections from the  $\rho^-$  cross sections of Fig. 21 suffer a spectacular attention as dipion mass increases across the  $\rho$  region. If this phenomenon proves to be generally true for vector exchanges, its interpretation may lead to new insight into particle-exchange mechanisms.

#### ACKNOWLEDGMENTS

We are grateful to the staff of the Argonne ZGS for assistance and encouragement during the course of the experiment. We would like to thank Marc Ross and Frank Henyey for stimulating conversations. We are especially indebted to Gordon Kane for suggesting the use of the Born amplitudes in our discussion of the mass dependence of the cross sections, and for a critical reading of part of the manuscript.

#### APPENDIX A: BORN AMPLITUDES FOR $\pi$ AND $\omega$ EXCHANGE

While the Born approximation does not give a realistic description of  $\rho$  production and decay,<sup>13</sup> it can be expected to give a crude indication of the relative dependence of production amplitudes of different helicities on production energy and on  $\rho$  mass. In Appendix A we outline a derivation of the energy and mass dependence of the Born amplitudes in the high-energy limit ( $s \rightarrow \infty$ ).

The particles of interest are labeled as follows:

$$a(\pi^-) + b(\text{target proton}) \rightarrow c(\rho^-) + d(\text{recoil proton}),$$

where the  $\rho^-$  is assumed to be a stable spin-1 particle. The equations for energy and momentum conservation in the production center-of-mass system are then

$$\begin{aligned} a_0 + b_0 &= c_0 + d_0, \\ \vec{a} + \vec{b} &= \vec{c} + \vec{d} = 0. \end{aligned} \quad (A1)$$

If the components of the energy-momentum 4-vector are chosen as  $a_1 = a_x$ ,  $a_2 = a_y$ ,  $a_3 = a_z$ , and  $a_4 = ia_0$ , then  $s$  and  $t$  are related to the energy-momentum variables above by

$$\begin{aligned}
s &= -(a_\nu + b_\nu)(a_\nu + b_\nu) \\
&= (a_0 + b_0)^2, \\
t &= -(c_\nu - a_\nu)(c_\nu - a_\nu) \\
&= (c_0 - a_0)^2 - (\vec{c} - \vec{a})^2.
\end{aligned} \tag{A2}$$

The production amplitudes will depend, in addition to the variables above, on the helicities  $\lambda = \pm\frac{1}{2}$ ,  $\lambda' = \pm\frac{1}{2}$ ,  $\mu = -1, 0, +1$  for the target proton, recoil

proton, and  $\rho^-$ , respectively. The 12 independent helicity amplitudes,  $B_{\lambda'\lambda}^\mu$ , are reduced to six by the parity relationships<sup>22</sup>

$$\begin{aligned}
B_{+1-}^{\pm 1} &= -B_{-1+}^{\mp 1}, & B_{+1+}^{\pm 1} &= B_{-1-}^{\mp 1}, \\
B_{+0-}^0 &= B_{-0+}^0, & B_{+0+}^0 &= -B_{-0-}^0.
\end{aligned} \tag{A3}$$

Using the notation above, one finds<sup>26</sup> the helicity projections of the invariant Born amplitudes for the diagram of Fig. 23 to be:

$\pi$  exchange,

$$B_{\lambda'\lambda}^\mu = if_{PPV} 2\epsilon_\nu^{(\mu)*} a_\nu (\pi^2 - t)^{-1} G_{BBP} \bar{U}_{(a)}^\lambda \gamma_5 U_{(b)}^\lambda; \tag{A4}$$

$\omega$  exchange,

$$B_{\lambda'\lambda}^\mu = \frac{f_{PVV}}{\rho} \epsilon_{\tau\nu\rho\sigma} a_\nu e_\rho \epsilon_\sigma^{(\mu)*} \left( \delta_{\tau\tau'} + \frac{e_\tau e_{\tau'}}{\omega^2} \right) (\omega^2 - t)^{-1} \bar{U}_{(a)}^\lambda \left( G_{BBV}^V \gamma_{\tau'} + \frac{G_{BBV}^T}{2N} \sigma_{\tau' \nu'} e_{\nu'} \right) U_{(b)}^\lambda.$$

The symbols  $\pi$ ,  $\rho$ ,  $\omega$ , and  $N$  in (A4) represent the masses of the  $\pi$ ,  $\rho$ ,  $\omega$ , and proton. The polarization vectors of the  $\rho$ ,  $\epsilon^\mu$ , and the Dirac spinors,  $U^\lambda$ , are represented explicitly below;  $e_\rho = c_\rho - a_\rho$  is the four-momentum of the exchanged particle; and  $\epsilon_{\tau\nu\rho\sigma}$  is defined by  $\epsilon_{1234} = 1$ ,  $\epsilon_{\tau\nu\rho\sigma} = 1$  for even permutations of 1234,  $-1$  for odd permutations, and zero otherwise.

The Born amplitudes can be evaluated as functions of the production polar angle  $\Theta$  of the  $\rho^-$  and the production energy and momentum by straightforward calculations from the explicit representations (valid when the azimuth angle of the  $\rho^-$  in the production center-of-mass system is  $\phi = 0$ ),

$$\begin{aligned}
U_{(b)}^+ &= \begin{pmatrix} 0 \\ -(b_0 + N)^{1/2} \\ 0 \\ -(b_0 - N)^{1/2} \end{pmatrix}, & U_{(b)}^- &= \begin{pmatrix} (b_0 + N)^{1/2} \\ 0 \\ -(b_0 - N)^{1/2} \\ 0 \end{pmatrix}, \\
\bar{U}_{(a)}^+ &= ((d_0 + N)^{1/2} \sin \frac{1}{2} \Theta, -(d_0 + N)^{1/2} \cos \frac{1}{2} \Theta, -(d_0 - N)^{1/2} \sin \frac{1}{2} \Theta, (d_0 - N)^{1/2} \cos \frac{1}{2} \Theta), \\
\vec{\gamma} &= \begin{pmatrix} 0 & -i\vec{\sigma} \\ i\vec{\sigma} & 0 \end{pmatrix}, & \gamma_4 &= \begin{pmatrix} 1 & 0 \\ 0 & -1 \end{pmatrix}, & \gamma_5 &= \begin{pmatrix} 0 & -1 \\ -1 & 0 \end{pmatrix}, & \sigma_x &= \begin{pmatrix} 0 & 1 \\ 1 & 0 \end{pmatrix}, & \sigma_y &= \begin{pmatrix} 0 & -i \\ i & 0 \end{pmatrix}, & \sigma_z &= \begin{pmatrix} 1 & 0 \\ 0 & -1 \end{pmatrix}, \\
\epsilon^{(+1)} &= \frac{1}{\sqrt{2}} \begin{pmatrix} -\cos\Theta \\ -i \\ \sin\Theta \\ 0 \end{pmatrix}, & \epsilon^{(0)} &= \begin{pmatrix} (C_0/\rho) \sin\Theta \\ 0 \\ (C_0/\rho) \cos\Theta \\ ic/\rho \end{pmatrix}, & \epsilon^{(-1)} &= \frac{1}{\sqrt{2}} \begin{pmatrix} \cos\Theta \\ -i \\ -\sin\Theta \\ 0 \end{pmatrix}.
\end{aligned} \tag{A5}$$

Evaluation of the tensor part of the  $\omega$ -exchange amplitude is facilitated by the identity<sup>26</sup>

$$\frac{G_{BBV}^T}{2N} \bar{U} \sigma_{\mu\nu} e_\nu U = G_{BBV}^T \bar{U} \gamma_\mu U + i \frac{G_{BBV}^T}{2N} (b_\mu + d_\mu) \bar{U} U. \tag{A6}$$

The equations above lead to the following amplitudes due to  $\pi$  and  $\omega$  exchange:

$$\begin{aligned}
B_{+1+}^+ &= \sqrt{2} K_P a \epsilon \beta_- \sin\Theta \cos \frac{1}{2} \Theta - \sqrt{2} \frac{K_V}{\rho} \epsilon [(\alpha_+ c_a - g \alpha_- c_a W/N) \cos^2(\frac{1}{2} \Theta) + \beta_+ c_a \alpha_0 + \beta_+ c_0 a \sin^2(\frac{1}{2} \Theta)] \sin \frac{1}{2} \Theta, \\
B_{+1-}^+ &= \sqrt{2} K_P a \epsilon \beta_+ \sin\Theta \sin \frac{1}{2} \Theta - \sqrt{2} \frac{K_V}{\rho} \epsilon [(\alpha_- c_a - g \alpha_+ c_a W/N) \sin^2(\frac{1}{2} \Theta) - \beta_- c_a \alpha_0 + \beta_- c_0 a \cos^2(\frac{1}{2} \Theta)] \cos \frac{1}{2} \Theta, \\
B_{+1+}^- &= -\sqrt{2} K_P a \epsilon \beta_- \sin\Theta \cos \frac{1}{2} \Theta - \sqrt{2} \frac{K_V}{\rho} \epsilon (\alpha_+ c_a - g \alpha_- c_a W/N + \beta_+ c_0 a) \cos^2(\frac{1}{2} \Theta) \sin \frac{1}{2} \Theta, \\
B_{+1-}^- &= -\sqrt{2} K_P a \epsilon \beta_+ \sin\Theta \sin \frac{1}{2} \Theta - \sqrt{2} \frac{K_V}{\rho} \epsilon (\alpha_- c_a - g \alpha_+ c_a W/N + \beta_- c_0 a) \sin^2(\frac{1}{2} \Theta) \cos \frac{1}{2} \Theta, \\
B_{0+}^0 &= 2K_P c_0 a \epsilon \beta_- \rho^{-1} (\cos\Theta - c_a/c_0 a) \cos \frac{1}{2} \Theta - 2 \frac{K_V}{\rho} \epsilon \beta_+ a \rho \sin^2(\frac{1}{2} \Theta) \cos \frac{1}{2} \Theta, \\
B_{0-}^0 &= 2K_P c_0 a \epsilon \beta_+ \rho^{-1} (\cos\Theta - c_a/c_0 a) \sin \frac{1}{2} \Theta + 2 \frac{K_V}{\rho} \epsilon \beta_- a \rho \sin^2(\frac{1}{2} \Theta) \cos \frac{1}{2} \Theta,
\end{aligned} \tag{A7}$$

with

$$\begin{aligned} W &= \sqrt{s}, \quad \epsilon = [(d_0 + N)(b_0 + N)]^{1/2}, \\ \beta_{\pm} &= \frac{d}{d_0 + N} \pm \frac{b}{b_0 + N}, \quad \alpha_{\pm} = 1 \pm \frac{bd}{\epsilon^2}, \\ K_P &= if_{PPV} G_{BBP} (\pi^2 - t)^{-1}, \\ K_V &= if_{PVV} (G_{BBV}^V + G_{BBV}^T) (\omega^2 - t)^{-1}, \end{aligned} \quad (\text{A8})$$

and

$$g = \frac{G_{BBV}^T}{G_{BBV}^V + G_{BBV}^T}.$$

In order to exhibit the dominant mass and energy dependence of the Born amplitudes, each amplitude is expanded in a power series in  $s^{-1}$  and only the leading power of  $s^{-1}$  is retained. The error introduced by omitting the higher powers in  $s^{-1}$  is typically  $\sim 10\%$  at 5 GeV. Equation (A7) becomes

$$\begin{aligned} B_{++}^1 &\cong -\sqrt{2} K_P N (\rho^2 - \pi^2) s^{-1} \sqrt{-t} - \frac{1-g}{\sqrt{2}} \frac{K_V}{\rho} s \sqrt{-t}, \\ B_{+-}^1 &\cong \sqrt{2} K_P (-t) + \frac{g}{2\sqrt{2}} \frac{K_V}{\rho} s N^{-1} (-t), \\ B_{++}^{-1} &\cong \sqrt{2} K_P N (\rho^2 - \pi^2) s^{-1} \sqrt{-t} - \frac{1-g}{\sqrt{2}} \frac{K_V}{\rho} s \sqrt{-t}, \\ B_{+-}^{-1} &\cong -\sqrt{2} K_P (-t) + \frac{g}{2\sqrt{2}} \frac{K_V}{\rho} s N^{-1} (-t), \\ B_{++}^0 &\cong -K_P \frac{\rho^2 - \pi^2}{\rho} N s^{-1} (\rho^2 - \pi^2 + t) - \frac{K_V}{\rho} \rho (-t), \\ B_{+-}^0 &\cong K_P \frac{\rho^2 - \pi^2 + t}{\rho} \sqrt{-t} - \frac{K_V}{\rho} \rho N (\rho^2 - \pi^2) s^{-1} \sqrt{-t}. \end{aligned} \quad (\text{A9})$$

The quantities  $N'\rho$ , proportional to the partial cross sections, are found from the definitions

$$N'\rho_{\mu\mu'} = \sum_{\lambda\lambda'} B_{\lambda'\lambda}^{\mu} B_{\lambda\lambda'}^{\mu'*}, \quad (\text{A10})$$

with

$$N' = \sum_{\mu} N'\rho_{\mu\mu}.$$

Equations (A10) can be simplified by explicit use of the parity relations (A3) and the Hermitian properties of the  $N\rho$  apparent from Eq. (A10). The resulting equations are

$$\begin{aligned} N'\rho_{11}^H &= |B_{++}^1|^2 + |B_{+-}^{-1}|^2 + |B_{+-}^1|^2 + |B_{++}^{-1}|^2, \\ N'\rho_{1-1}^H &= 2 \operatorname{Re}(B_{++}^1 B_{+-}^{-1*}) + 2 \operatorname{Re}(B_{+-}^1 B_{++}^{-1*}), \\ N'\rho_{10}^H &= (B_{++}^1 - B_{+-}^{-1}) B_{++}^{0*} + (B_{+-}^1 - B_{++}^{-1}) B_{+-}^{0*}, \\ N'\rho_{00}^H &= 2 |B_{++}^0|^2 + 2 |B_{+-}^0|^2, \\ N' &= 2N'\rho_{11}^H + N'\rho_{00}^H. \end{aligned} \quad (\text{A11})$$

The dominant  $s$  and  $\omega$  dependence of the  $N\rho$ 's fol-

lows from dropping, in Eq. (A9),  $\pi$ -exchange amplitudes of order lower than  $s^0$ - and  $\omega$ -exchange amplitudes of order lower than  $s^1$ , and substituting the resulting amplitudes in Eq. (A11). One finds

$$\begin{aligned} N'\rho_{11}^H &= 4|K_P|^2 (-t)^2 \\ &\quad + \frac{|K_V|^2}{\rho^2} s^2 \left( (1-g)^2 (-t) + \frac{g^2}{4N^2} (-t)^2 \right), \\ N'\rho_{1-1}^H &= -4|K_P|^2 (-t)^2 \\ &\quad + \frac{|K_V|^2}{\rho^2} s^2 \left( (1-g)^2 (-t) + \frac{g^2}{4N^2} (-t)^2 \right), \\ N'\rho_{10}^H &= 2\sqrt{2} |K_P|^2 \rho^{-1} (\rho^2 - \pi^2 + t) (-t)^{3/2}, \\ N'\rho_{00}^H &= 2|K_P|^2 \rho^{-2} (\rho^2 - \pi^2 + t)^2 (-t). \end{aligned} \quad (\text{A12})$$

Finally, we rearrange the first two of Eqs. (A12) by expressing  $g$  in terms of its definition in (A8), and retaining only the leading terms in  $t/\rho^2$  for small  $t$ . The results are given in Eqs. (11) and (12) of the text.

#### APPENDIX B: DETERMINATION OF DENSITY-MATRIX ELEMENTS FROM THE MOMENTS OF MALAMUD AND SCHLEIN

We have used data from the bubble-chamber compilation of Malamud and Schlein<sup>11</sup> in our discussion of the asymmetry parameter and the mass dependence of the density-matrix elements. Their data are presented in the form of plots of spherical harmonic moments of the dipion angular distribution as a function of dipion mass  $\omega$  for  $t > -0.16$ . This appendix explains the procedure that we have used to extract density-matrix elements from their data.

The spherical harmonic moment of  $Y_l^m(\theta, \phi)$  is defined by

$$N \langle Y_l^m \rangle = \int \frac{dN}{d\Omega_{\pi\pi}} Y_l^{m*} d\Omega_{\pi\pi}, \quad (\text{B1})$$

$$N = \int \frac{dN}{d\Omega_{\pi\pi}} d\Omega_{\pi\pi}.$$

Inspection of Eq. (8) of the text shows that the data should require moments up to only  $l=2$  to describe the data, and this is found experimentally to be the case.<sup>11</sup> We use a phase convention for the spherical harmonics for which only  $Y_1^1$  and  $Y_2^2$  contain the phase  $(-1)$ , while all other relevant harmonics contain the phase  $(+1)$ . We then find by applying Eq. (B1) to  $dN/d\Omega_{\pi\pi}$  given in Eq. (10) of the text that

$$\begin{aligned} N\rho_{00} + 2N\rho_{11} + N\rho_s &= N \langle 1 \rangle = N, \\ N\rho_{00} - N\rho_{11} &= (5\pi)^{1/2} N \langle Y_2^0 \rangle, \\ N \operatorname{Re} \rho_{10} &= (5\pi/3)^{1/2} N \langle Y_2^1 \rangle, \\ N\rho_{1-1} &= -(10\pi/3)^{1/2} N \langle Y_2^2 \rangle. \end{aligned} \quad (\text{B2})$$

The density-matrix elements  $N\rho_{00}$  and  $N\rho_{11}$  can be determined only if the  $s$ -wave contribution is known. To determine the  $\rho^-$  moments for the Malamud-Schlein data, we assume that  $\rho_s = 0$ . Our reasons are explained in Sec. IX of the text. For the  $\rho^0$  moments, we assume  $\rho_s = 0.2$  independent of  $\omega$  and  $t$ . Within the uncertainties of this determination, this is the same as the value determined for the  $\rho$  mass region in several studies<sup>10,14</sup> of  $\rho^0$  production in  $\pi^-p \rightarrow \pi^-\pi^+n$ . We assume no dependence on  $\omega$  because the preferred phase shifts of Ref. 21 give about the same  $\omega$  dependence for  $s$  and  $p$  waves on the mass shell. When the value  $\rho_s = 0.2$  is used in Eqs. (B2) with the moment data from Ref. 11, the partial cross sections shown in Fig. 21 result.

### APPENDIX C

The helicity and Gottfried-Jackson frames have both been used in this article as reference axes for the density-matrix elements. An explicit transformation between the density-matrix elements in these two frames is derived in this appendix. This transformation has been used as a check on the least-squares fits obtained independently in the two frames, and as an aid in interpreting theoretical expressions for the density-matrix elements in the two frames.

Let the amplitude for producing a dipion with angular momentum  $l$  and helicity  $\mu$  be  $F_{\lambda'\lambda}^{\mu}$ , where  $\lambda'\lambda$  are the recoil and target proton helicities. If dipion decay is independent of production, then angular momentum conservation requires the overall amplitude for finding the decay pions at  $\theta, \phi$  in the  $\rho$  rest frame to be

$$\begin{aligned} A^\mu &= F_{\lambda'\lambda}^{\mu} f(\omega) Y_l^\mu(\theta, \phi) \\ &\equiv M_{\lambda'\lambda}^{\mu} Y_l^\mu, \end{aligned}$$

where  $f(\omega)$  contains the effects of decay dynamics. This amplitude must be summed over indistinguishable ways of observing  $\theta, \phi$ , that is, summed over  $l$  and  $\mu$  for given  $\lambda'\lambda$  in order to get the total amplitude  $A$ . The cross section is then found by summing  $AA^*$  over  $\lambda$  and  $\lambda'$  and multiplying by phase space. We write the result as

$$\frac{dN}{d\Omega_{\pi\pi}} = P_{(s,\omega)} \sum_{\mu\mu'} \rho_{\mu\mu'}(s, t, \omega) Y_l^\mu Y_l^{\mu'*}, \quad (C1)$$

where the density matrix  $\rho$  is given by

$$\rho_{\mu\mu'} = \sum_{\lambda\lambda'} M_{\lambda\lambda'}^{\mu} M_{\lambda\lambda'}^{\mu'*}, \quad (C2)$$

and  $P$  is a phase-space factor invariant under rotations.

Now consider a rotation by  $\psi$  about the  $y$  axis of Fig. 15, taking the Gottfried-Jackson frame into the helicity frame. From the spherical trigonometry of the triangle  $\hat{b}, -\hat{r}, \hat{\pi}^-$ , one finds

$$\begin{aligned} Y_0^{(GJ)} &= Y_0^{(H)}, \\ Y_1^{0(GJ)} &= \frac{\sin\psi}{\sqrt{2}} Y_1^{1(H)} + \cos\psi Y_1^{0(H)} - \frac{\sin\psi}{\sqrt{2}} Y_1^{-1(H)}, \\ Y_1^{1(GJ)} &= \frac{1}{2}(1 + \cos\psi) Y_1^{1(H)} - \frac{\sin\psi}{\sqrt{2}} Y_1^{0(H)} \\ &\quad + \frac{1}{2}(1 - \cos\psi) Y_1^{-1(H)}, \\ Y_1^{-1(GJ)} &= \frac{1}{2}(1 - \cos\psi) Y_1^{1(H)} + \frac{\sin\psi}{\sqrt{2}} Y_1^{0(H)} \\ &\quad + \frac{1}{2}(1 + \cos\psi) Y_1^{-1(H)}. \end{aligned} \quad (C3)$$

To find the transformation equations for the density-matrix elements, we write out Eq. (C1) in the Gottfried-Jackson frame, replace the  $Y_l^{m(GJ)}$  from Eq. (C3), collect coefficients of  $Y_l^{\mu(H)} Y_l^{\mu'(H)*}$ , and equate to the coefficients of the same expression from Eq. (C1) in the helicity frame. The result is

$$\begin{aligned} \rho_{00}^H &= \cos^2\psi \rho_{00}^{GJ} - 2\sqrt{2} \sin\psi \cos\psi \operatorname{Re} \rho_{10}^{GJ} \\ &\quad + \sin^2\psi \rho_{11}^{GJ} - \sin^2\psi \rho_{1-1}^{GJ}, \\ \operatorname{Re} \rho_{10}^H &= \frac{\sin\psi \cos\psi}{\sqrt{2}} \rho_{00}^{GJ} + (\cos^2\psi - \sin^2\psi) \operatorname{Re} \rho_{10}^{GJ} \\ &\quad - \frac{\sin\psi \cos\psi}{\sqrt{2}} \rho_{11}^{GJ} + \frac{\sin\psi \cos\psi}{\sqrt{2}} \rho_{1-1}^{GJ}, \\ \rho_{11}^H &= \frac{\sin^2\psi}{2} \rho_{00}^{GJ} + \sqrt{2} \sin\psi \cos\psi \operatorname{Re} \rho_{10}^{GJ} \\ &\quad + \frac{1 + \cos^2\psi}{2} \rho_{11}^{GJ} + \frac{\sin^2\psi}{2} \rho_{1-1}^{GJ}, \\ \rho_{1-1}^H &= -\frac{\sin^2\psi}{2} \rho_{00}^{GJ} - \sqrt{2} \sin\psi \cos\psi \operatorname{Re} \rho_{10}^{GJ} \\ &\quad + \frac{\sin^2\psi}{2} \rho_{11}^{GJ} + \frac{1 + \cos^2\psi}{2} \rho_{1-1}^{GJ}, \\ \operatorname{Re} \rho_{s0}^H &= \cos\psi \operatorname{Re} \rho_{s0}^{GJ} - \sqrt{2} \sin\psi \operatorname{Re} \rho_{s1}^{GJ}, \\ \operatorname{Re} \rho_{s1}^H &= \frac{\sin\psi}{\sqrt{2}} \operatorname{Re} \rho_{s0}^{GJ} + \cos\psi \operatorname{Re} \rho_{s1}^{GJ}. \end{aligned} \quad (C4)$$

The angle  $\psi$  is readily evaluated by combining expressions for the Lorentz invariants  $s, t, P_\rho, P_b \cdot P_r$ , and  $P_B \cdot P_T$ , where  $P_\rho, P_r, P_b$ , and  $P_T$  are the four-momenta of the  $\rho$ , recoil proton, beam  $\pi^-$ , and target proton, respectively, in the  $\rho$  rest frame. One finds

$$\cos\psi = \frac{2\rho^2(s+t-\rho^2-N^2) - (s-\rho^2-N^2)(\pi^2+\rho^2-t)}{\{[t-(\rho-\pi)^2][t-(\rho+\pi)^2][s-(\rho-N)^2][s-(\rho+N)^2]\}^{1/2}}, \quad (C5)$$

with the convention used earlier that the symbol for a particle represents the mass of that particle.

The angle  $\psi$  and the off-diagonal transformation coefficients in Eq. (C4) become quite large for the larger values of  $-t$  of this experiment. For example, for  $\rho = 760 \text{ MeV}/c^2$  and  $-t = 0.35 \text{ (GeV}/c)^2$ ,  $\psi = 80^\circ$ . It is apparently only an accident that the values of  $\rho_{00}^H$  and  $\rho_{00}^{GJ}$  given in Tables IV and V are not more different than they are.

As a final point, we note that in the high-energy limit,  $\psi$  depends only on  $t$  and  $\rho$ , not on  $s$ . Ex-

plicitly,

$$\cos\psi \cong \frac{1+t/\rho^2}{1-t/\rho^2}, \quad \sin\psi \cong 2\left(\frac{-t}{\rho^2}\right)^{1/2} \left(1 + \frac{t}{\rho^2}\right). \quad (\text{C6})$$

Equation (C6) shows that a density-matrix element  $N\rho^H$  in Eq. (8) of the text will transform into an element containing the same power of  $s$  in the Gottfried-Jackson frame. This fact verifies the remark made at the end of Sec. IX that elementary particle  $\omega^0$  exchange alone gives  $\rho_{11} = \rho_{1-1} = \frac{1}{2}$  in both frames in the high-energy limit.

\*Work supported by the U. S. Atomic Energy Commission.

†Present address: Oberlin College, Oberlin, Ohio 44074.

‡Present address: Bendix Corporation, Ann Arbor, Mich. 48104.

§Present address: Esso Production Research Laboratory, Houston, Tex.

|| Present address: Bendix Corporation, Ann Arbor, Mich. 48104.

\*\*Present address: Physics Department, Ohio State University, Columbus, Ohio 43210.

<sup>1</sup>A. R. Erwin, R. March, W. D. Walker, and E. West, *Phys. Rev. Letters* **6**, 628 (1961).

<sup>2</sup>Saclay-Orsay-Bari-Bologna Collaboration, *Nuovo Cimento* **25**, 365 (1962).

<sup>3</sup>Aachen-Birmingham-Bonn-Hamburg-London-München Collaboration, *Nuovo Cimento* **31**, 729 (1964).

<sup>4</sup>E. West, J. H. Boyd, A. R. Erwin, and W. D. Walker, *Phys. Rev.* **149**, 1089 (1966).

<sup>5</sup>V. Hagopian and Y. Pan, *Phys. Rev.* **152**, 1183 (1966).

<sup>6</sup>D. H. Miller, L. Gutay, P. B. Johnson, F. J. Loeffler, R. L. McIlwain, R. J. Sprafka, and R. B. Willmann, *Phys. Rev.* **153**, 1423 (1967).

<sup>7</sup>R. L. Eisner, P. B. Johnson, P. R. Klein, R. E. Peters, R. J. Sahni, W. L. Yen, and G. W. Taufest, *Phys. Rev.* **164**, 1699 (1967).

<sup>8</sup>J. P. Baton and G. Laurens, *Phys. Rev.* **176**, 1574 (1968).

<sup>9</sup>S. J. Barish, W. Selove, N. N. Biswas, N. M. Cason, P. B. Johnson, V. P. Kenney, J. A. Poirer, W. D. Shephard, and H. Yuta, *Phys. Rev.* **184**, 1375 (1969).

<sup>10</sup>B. Y. Oh, A. F. Garfinkel, R. Morse, W. D. Walker, J. D. Prentice, E. C. West, and T. S. Yoon, *Phys. Rev. D* **1**, 2494 (1970).

<sup>11</sup>E. Malamud and P. Schlein, in *Proceedings of the Conference on  $\pi\pi$  and  $K\pi$  Interactions, Argonne National Laboratory, 1969*, edited by F. Loeffler and E. D. Malamud (Argonne National Laboratory, Argonne, Ill., 1969), p. 93.

<sup>12</sup>J. H. Scharenguivel, in *Proceedings of the Conference on  $\pi\pi$  and  $K\pi$  Interactions, Argonne National Laboratory, 1969*, edited by F. Loeffler and E. D. Malamud (Argonne National Laboratory, Argonne, Ill., 1969), p. 306.

<sup>13</sup>K. Gottfried and J. D. Jackson, *Nuovo Cimento* **34**, 735 (1964); M. H. Ross and G. L. Shaw, *Phys. Rev.*

*Letters* **12**, 627 (1964); L. Durand III and Y. T. Chiu, *Phys. Rev.* **139**, B646 (1965); J. D. Jackson, *Rev. Mod. Phys.* **37**, 484 (1965).

<sup>14</sup>F. Bulos, R. K. Carnegie, G. E. Fischer, E. E. Kluge, D. W. G. S. Leith, H. L. Lynch, B. Ratcliff, B. Richter, H. H. Williams, and S. H. Williams, *Phys. Rev. Letters* **26**, 1457 (1971); P. Baillon, *et al.*, *Phys. Letters* **35B**, 453 (1971).

<sup>15</sup>See, for example, K. Gottfried and J. D. Jackson, *Nuovo Cimento* **33**, 309 (1964).

<sup>16</sup>An earlier version of MASS is described in A. Saulys, D. Meyer, and R. Allen, *Nucl. Instrum. Methods* **39**, 335 (1966).

<sup>17</sup>C. T. Coffin, N. Dikmen, L. Ettlinger, D. Meyer, A. Saulys, K. Terwilliger, and D. Williams, *Phys. Rev.* **159**, 1169 (1967).

<sup>18</sup>H. Messel and D. F. Crawford, *Electron-Photon Shower Distribution Function* (Pergamon, New York, 1970), p. 1260.

<sup>19</sup>Jan Pisut and Matts Roos, *Nucl. Phys.* **B6**, 325 (1968).

<sup>20</sup>Particle Data Group, *Rev. Mod. Phys.* **42**, 87 (1970).

<sup>21</sup>J. D. Jackson, J. T. Donohue, K. Gottfried, R. Keyser, and B. E. Y. Svensson, *Phys. Rev.* **139**, B428 (1965).

<sup>22</sup>See, for example, Ref. 11.

<sup>23</sup>See, for example, L. J. Gutay, in *Proceedings of the Conference on  $\pi\pi$  and  $K\pi$  Interactions, Argonne National Laboratory, 1969*, edited by F. Loeffler and E. D. Malamud (Argonne National Laboratory, Argonne, Ill., 1969), p. 241.

<sup>24</sup>We are indebted to G. L. Kane for emphasizing this virtue of the helicity frame and for encouraging us to use it in our analysis.

<sup>25</sup>J. H. Scharenguivel *et al.*, *Phys. Rev. Letters* **24**, 332 (1970).

<sup>26</sup>H. Pilkuhn, *The Interactions of Hadrons* (Wiley, New York, 1967), p. 282.

<sup>27</sup>H. P. Dürr and H. Pilkuhn, *Nuovo Cimento* **40**, 899 (1965).

<sup>28</sup>W. L. Yen *et al.*, *Phys. Rev. Letters* **18**, 1091 (1967).

<sup>29</sup>G. L. Kane, F. Henyey, D. R. Richards, and Marc Ross, *Phys. Rev. Letters* **25**, 1519 (1970).

<sup>30</sup>F. Henyey, G. L. Kane, Jon Pumplin, and M. H. Ross, *Phys. Rev.* **182**, 1579 (1969).